Fluorescence lifetimes and refractometric sensing with cavity-coupled silicon quantum dots

by

Deborah Kwok-Yee Chung

A thesis submitted in partial fulfillment of the requirements for the degree of

Master of Science

Department of Physics
University of Alberta

Abstract

This thesis explores the dynamics and sensing performance of silicon quantum dot (SiQD) ensembles coupled to the whispering gallery modes (WGMs) of spherical and cylindrical microcavities. The first project investigated the possibility of observing Purcell effects in an ensemble of QDs coupled to a microsphere resonator. However, no convincing evidence for rate modifications was found. Several possible reasons for this negative result were outlined and future experimental improvements were suggested. Next, the SiQDs were coupled to the WGMs of cylindrical cavities (fibers and microcapillaries) in order to investigate and optimize their refractive-index sensing performance. These sensors register a WGM wavelength shift in response to changes in local index of refraction. Using an SiQD coated optical fiber, the detection limit of the sensor was improved by projecting the WGM spectrum onto a full 2 dimensional CCD array. However, noise from various experimental sources limited the detection limit of the fiber sensor to a value of 2.4×10^{-3} RIU. In order to further improve the ultimate limit of detection, a more mechanically stable device was constructed. This consisted of a microcapillary whose channel was coated with a layer of SiQDs embedded in a protective oxide matrix. By controlling the SiQD channel film thickness via an etching procedure, the device sensitivity to refractometric changes was maximized. Using the techniques developed to minimize the wavelength shift resolution, a detection limit of 1.7×10^{-4} RIU was experimentally measured, which is less than a factor 2 larger than the calculated optimum theoretical limit of detection. This represents one of the best experimentally-observed detection limits reported for fluorescent WGM devices.

Acknowledgements

Contents

List of Figures

List of Tables

Chapter 1

Introduction

1.1 Optical methods of sensing

This thesis deals with structures that can perform refractometric sensing based on the "whispering gallery modes" (WGMs) in dielectric microcavities. Refractometric sensors can be used to measure small changes in the refractive index (RI) of a (microfluidic) analyte. Before discussing the basics of sensing with WGMs, we will give a brief overview of some of the more widely researched methods in the development of microfluidics-compatible optical sensors.

Sensing methods typically employ electrical, chemical, thermal, or optical mechanisms [10] to detect changes in a local analyte (*i.e.* in a fluid). Optical methods have some important advantages for sensing applications. For example, optical sensing methods are non-destructive, can have high signal-to-noise ratio, and can be relatively easily miniaturized (*via.* lenses, fiber optics, *etc.*) for integration into lab-on-a-chip systems. Optical methods also have fast response times, which permits the development of real-time detection devices. Designs for optical sensors are generally simple to fabricate and use inexpensive materials. Some optical methods also allow remote sensing [11, 12], in which the transducer can be distant from the detection system, allowing sensing in harsh or remote environments. The focus of this thesis is on refractometric optical sensing mechanisms, with a brief foray into cavity-induced emitter lifetime effects.

Optical sensing methods can be "labeled" or "non-labeled". A standard biological detection method is to label cells or other biological analytes with "tags" such as fluorescent dyes

or quantum dots [13, 14, 15]. Detection of fluorescence*, typically via an imaging system, indicates the presence of the analyte. This is a standard technique because it is sensitive (it can mark the presence of single particles), reproducible, and a large variety of fluorescent tags exist. The main drawbacks include photobleaching and the fact that prior preparation of the analyte is required [14, 15]. An alternative is to use "label-free" sensing methods, which do not require prior preparation of the analyte.

There are many powerful label-free methods for optical sensing. These methods can detect small local changes at the surface of the sensor, in the bulk analyte, or both [17]. Some methods can detect few or even single particles. Other sensors can be functionalized for detecting specific bio-molecules, eliminating the need for fluorescent labeling. Optical methods can also be combined in order to increase sensitivities and compensate for the particular drawbacks of each method [18, 19, 20, 21].

The limit of detection (LoD) for bulk refractometric sensors can be given in terms of "refractive index units" (RIU). For example, an LoD of 10^{-7} RIU is equivalent to detecting ~58 grains of table salt in 1 L of water. For biosensors on the other hand, one typically gives the LoD as a concentration or mass of an analyte. The sensitivity S of a sensor can be given in terms of the magnitude of the sensor response, and is typically defined as $S = \frac{d\lambda}{dRIU}$ for refractometric sensors. A few sensor types will next be briefly described and compared in terms of their sensitivity and LoD, in order to provide a comparison to the values measured for "whispering gallery mode" sensors which are characterized later in this work.

1.1.1 Interferometers

Interferometers, sometimes known as "evanescent wave" [12] or "evanescent field" [22] sensors, compare and monitor a reference signal and a measurement signal. In interferometric sensors, changes in an interference pattern are monitored during a detection event. The measurement signal corresponds to a change in the refractive index, while the reference signal is monitored to remove interactions not associated with the analyte [23]. They can have refrac-

---

*Fluorescence generally refers to emission from singlet recombination, as opposed to triplet recombination which has a much longer lifetime and is referred to as "phosphorescence". The general term "luminescence" (or "photoluminescence" for optical pumping) includes both fluorescence and phosphorescence. In silicon QDs the emission process, although characterized by a microsecond decay, is likely related to singlet recombination [16]. Therefore, in this work the term "fluorescence" will frequently be used.

tometric detection limits around 10^{-7} RIU [12]. Broadly defined, there are several different classes of interferometers including Mach-Zehnder interferometers, Young's (double-beam) interferometers, Fabry-Perot interferometers, and Hartman interferometers.

Mach-Zehnder interferometers (MZI)[1] are the possibly simplest interferometric sensors. A MZI consists of a waveguide that splits into two arms, one that passes through the analyte and one that acts as the reference (Fig. 1.1). The two arms recombine [24], and the interference pattern is observed. MZIs can be fabricated with standard micro-fabrication processes. One such fabricated MZI was used to monitor the dynamics of DNA strands in real time [25]. Real time rather than "delayed" detection is characteristic of MZI and Young's interferometers. The MZI has a low detection limit of 10^{-7} RIU [24, 26].

Young's or double-beam interferometers are based on the familiar concept of a double-slit interference. These devices are similar to MZI in that they have two different paths along which light travels (Fig. 1.1). One path passes through the analyte, and one passes through a reference medium. The two paths recombine *via* slit diffraction or beam divergence [24]. A change in the resulting interference pattern corresponds to a change in the refractive index of the analyte. These interferometers can take the form of planar waveguides [27], which are relatively easy and inexpensive to fabricate. They can detect nanomolar concentrations of protein and can have bulk detection limits of 10^{-5} RIU [27].

Fabry-Perot sensors are typically comprised of two distributed Bragg reflectors (DBRs) separated by a gap region. Fluid analyte is pumped into the gap, causing the resonant wavelength to shift. As such, they are similar to the sensors investigated later in this work. White light can be used to illuminate one surface of the FP cavity and the transmission or reflection spectra is monitored as a function of analyte concentration. They can be inexpensive to fabricate; for example, a Fabry-Perot interferometer can be made from relatively standard materials such as multilayer films or porous silicon [28]. When a molecule binds to the porous silicon network, the effective refractive index of the layer changes, and the interference spectrum changes accordingly. These sensors have detection limits as low as 10^{-9} RIU [29].

The Hartman interferometer [22] is a proprietary "evanescent wave sensor". It was designed with commercialization in mind by using existing semiconductor technologies to fabri-

3
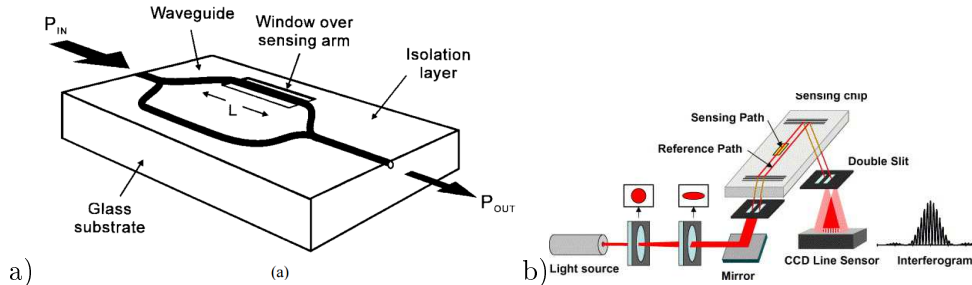
Figure 1.1: Diagrams illustrating a) a Mach-Zehnder interferometer (adapted from [1]) ; and b) a Young interferometer with grating couplers (adapted from [2]). In both configurations, incident light is split into two paths. One path samples the analyte and one acts as a reference signal. Both signals are recombined into an interference pattern which is then read out.

cate parallel waveguides as well as direct grating couplers. The inclusion of grating couplers simplifies the coupling of light into and out of the interferometer. The Hartman interferometer has a concentration detection limit on the order of ng /mL [22].

A major disadvantage of interferometric sensors is their large size, especially relative to competing lab-on-a-chip sensors. Since the light beam only passes through the analyte once (ie. single-pass), in order to achieve high sensitivity via a long interaction length, the interferometer itself must be usually centimeters long. This makes integrating the interferometer into microfluidic systems more difficult.

1.1.2 Photonic crystals

Photonic crystals (PhC) have been used to measure temperature [30, 31], humidity [32, 33], mechanical stress [34, 35], and the presence of gases [36, 37] as well as for biosensing [38, 39]. Their compact size and compatibility with standard silicon-on-insulator fabrication technologies make them suitable for lab-on-a-chip biosensing applications (Fig. 1.2). They can be used to detect nanometer-dimension bio-molecules and proteins due to their confinement of light in a small volume [40]. A photonic crystal sensor needs only small fluid volumes; for example, gaseous He and CO_2 were detected in a sample volume as small as 40 attolitres corresponding to 10^6 molecules [41]. Photonic crystals have typical detection limits of 10^{-5} RIU [41, 36]. They can be used to detect nanomolar [42] down to picomolar concentrations of proteins such as anti-biotin [43]. They can have excellent refractometric sensitivities, up to 510 nm/RIU [41] for an air slot PhC.

a) ... b)
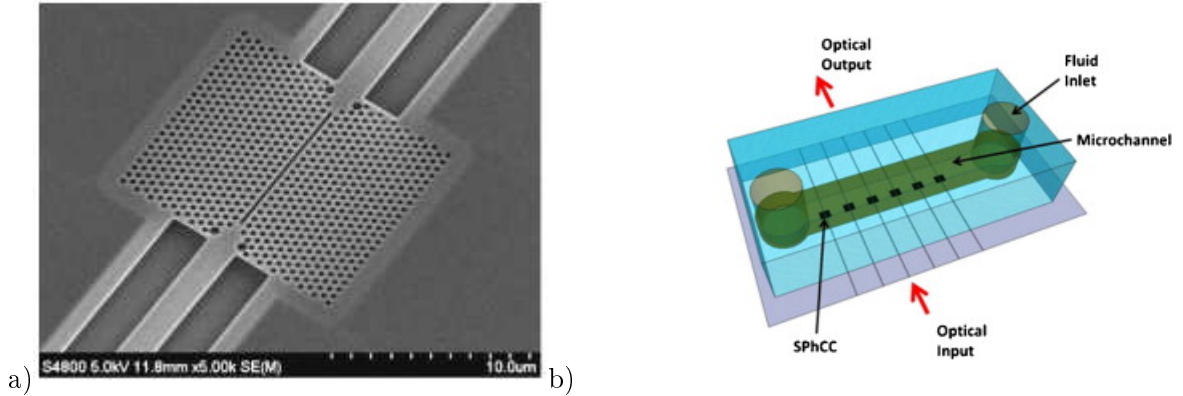
Figure 1.2: a) An SEM image of a slotted photonic crystal fabricated with silicon-on-insulator technologies. b) The sensing setup of several slot photonic crystal sensors in a fluidic setup. Reproduced from Ref. [3]

Photonic crystals can be 1-, 2- or 3-dimensional. They are made of a periodic lattice structure of contrasting refractive indices; a typical example being periodic air holes in a dielectric matrix. The geometry of the PhC lattice determines the wavelengths of light that pass through or are reflected from the lattice. The parameters that can be controlled are reflection angle or reflected wavelength [40]. The main sensing mechanism is a relative shift in one of these parameters. For example, a 1-dimensional gas sensor expands in the presence of analyte (greater distance between unit cells), which causes the cavity resonances to shift [44].

Photonic crystal fibers (PCF), also known as micro-structured optical fibers (MOF), operate by filling some of the air holes with the liquid or gas analyte, changing the effective refractive index in the core [45]. The PCF has been used as a gas sensor [46, 47], to measure strain and temperature [48, 49], and for biosensing applications [50]. A PCF can have sensitivities as high as 1400 nm/RIU [51] or even 38 000 nm/RIU in special cases [52].

Photonic crystals are easy to fabricate in large batches with standard silicon-on-insulator technologies, and can be integrated with other optical sensing methods [53]. However there are technical difficulties in controlling the fabrication and etching process (which often requires a time consuming serial method such as electron beam lithography) while minimizing loss [39].

1.1.3   Surface plasmon resonance (SPR) based sensors

A surface plasmon resonance (SPR) is the resonance of oscillating conduction electrons at the interface between a metal and a dielectric (Fig. 1.3). When the frequency of incident light on the metal is at or below the plasma frequency, the conduction electron resonance that forms at the metal surface is quantized as a plasmon. This resonance is formed at the interface between a dielectric and a thin metal film when incident light excites free electrons in the conductor and at the appropriate plasmon resonance frequency. The plasmon wave is a transverse wave that travels along the interface, so it is polarized (specifically transverse magnetic polarized). These plasmons can be localized on nanoparticles or propagate as waves in a metallic thin film.

SPR sensors monitor the shift in the plasmon resonance wavelength due to a change in the refractive index of the dielectric material (*i.e.* in a fluid) adjacent to the metal dielectric interface. Surface plasmon resonance sensors are a well developed technology with high sensitivities and low detection limits. There are several commercially available SPR-based sensors for biodetection [54]. The first commercial example[†] was marketed by BIAcore in 1990. Recently, "hand-held" cell-phone based SPR sensors were demonstrated [55, 56] though they are yet commercialized. Commercial SPR devices have high sensitivity up to $\sim 500\,\text{nm}/\text{RIU}$ and ultimate bulk detection limits down to $10^{-7}\,\text{RIU}$ [57]. SPR devices can also be produced and integrated in large numbers (multiplexed).

While SPR sensors are among the most advanced optical sensing technologies, some drawbacks remain. For example, SPR-based devices are not ideally suited for lab-on-a-chip or other integrated technologies, because they have tended to be relatively large and bulky. Efforts are therefore being made to miniaturize such devices [4]. Because of the lossy nature of the surface plasmon, an SPR can have a large linewidth and low signal-to-noise ratio, limiting the device sensitivity and resolution. Finally, commercial SPR devices can be fairly expensive [57, 58].

[†]www.biacore.com
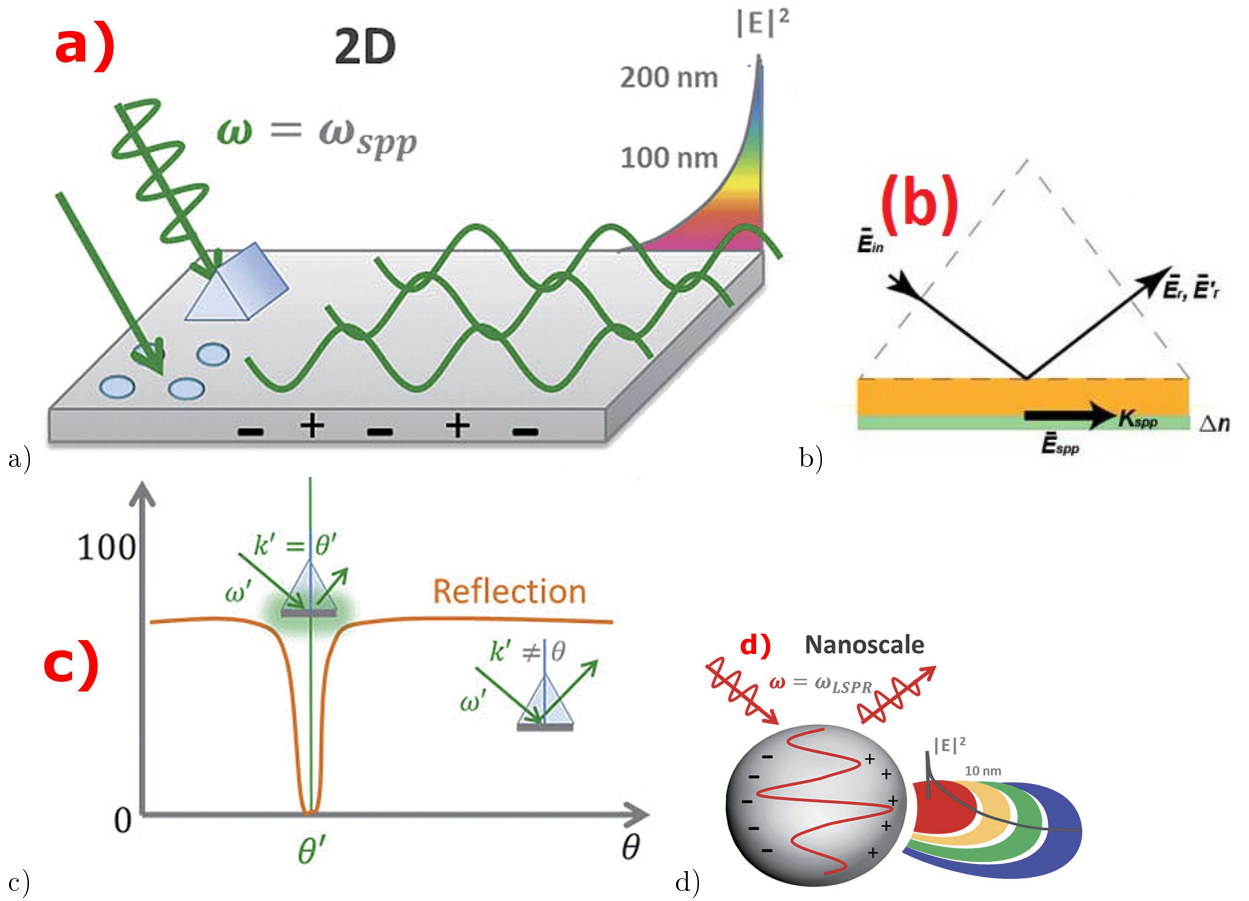
Figure 1.3: Schematics illustrating the workings of SPR-type sensors. a) TM polarized incident light couples into propagating surface plasmons in a metal film when the incident wavevector and momentum matches the wavevector and momentum of the plasmon. b) A common method of varying the incident photon momentum is by changing the angle of incidence with a prism coupler. This is known as the Kretschmann configuration. c) When the resonance conditions are met, the intensity of reflected light is lower than off-resonance. d) Diagram of a localized surface plasmon resonance (LSPR) on a nanoparticle. The EM field is also locally amplified. Images a), c), d) are reproduced from Ref. [4], whereas b) is from Ref. [5]

1.1.4 Surface-enhanced Raman scattering (SERS) based sensors

Surface-enhanced Raman scattering (SERS) enhances the signal of a Raman spectrum from an analyte [4]. A Raman spectrum is a spectrum obtained through a scattering process analogous to Rayleigh scattering, but instead of the same photon energy being scattered, some energy is transferred between the analyte and the electric field. The emerging radiation either loses energy (lower frequency) to the analyte as phonons, or gains energy (higher frequency) from the analyte. This results in discrete lines forming a characteristic spectrum [59]. Localized surface plasmons can enhance both the incident excitation and the Raman scattered fields [60]. SERS enhances the Raman field by as much as 14 to 15 orders of magnitude, which makes it a good technique to detect single molecules [61]. The concentration detection limit of SERS is on the scale of nM.

1.1.5 Waveguides and fiber optic sensors

Aside from facilitating other optical sensing methods, waveguides can also be developed as optical senors themselves. One example is the spiral waveguide [62], which is effectively a type of ring resonator. A change in the effective refractive index by adsorption of a molecule on the resonator surface changes the wavelength of the resonances in a transmission spectrum. The electric field density is high at the core of the waveguide, which has a high index contrast and a small cross-section. This gives the sensor sensitivity to surface adsorption.

Spiral waveguide sensors can be advantageously combined with slot waveguides [63, 64, 65]. Slot waveguide sensors [66] consist of two high-refractive-index waveguides that are positioned close to one another, such that the low index "slot" between them is less than a wavelength in width. The electric field density is very high in the slot, which makes it attractive for sensing. They can have sensitivies of 200 to 300 nm/RIU and detection limits of 10^{-4} to 10^{-5} RIU [63, 66].

Fiber optic sensors are the subject of a massive body of literature *e.g.* [17, 20, 67] and are found in a large range of applications, including temperature [68], pH [69], and concentration [70] sensors, as well as in biosensing [67] and chemical sensing [71, 72]. There are many possible transduction mechanisms for a fiber optic sensor. They can be used in interferometer

configurations [73, 74], or the transmission, absorption, or reflectance of a pump laser can be monitored at either end of the fiber. As well, the fiber can be coated with a fluorescent coating whose emission spectrum depends on the chemical properties of the surroundings [71]. One of the sensors described later in this work is a fiber-optic fluorescence-based sensor. Another configuration is fiber loop ringdown spectroscopy [75, 76], in which absorption in an analyte shortens the characteristic ringdown time for light circulating in a fiber loop. Other configurations can include Bragg gratings [77], or photonic crystals in microstructured fibers [53]. Bulk detection limits can be in the range of 10^{-6} to 10^{-7} RIU [75, 77] and refractometric sensitivities can be as high as 1394 nm/RIU [77]. One advantage of fiber-based sensors is that they can easily be adopted to remote sensing, where the transducing part of the sensor can be in an extreme environment [11, 73] or in a hard-to-reach location [40].

1.2   Introduction to whispering gallery modes

The sensors investigated in this work are whispering gallery mode optical resonators. The term "whispering gallery mode" was originally coined to describe a peculiar acoustic phenomenon reported to occur in the circular dome of St. Paul's Cathedral in London. According to Lord Rayleigh's original paper [78], the cathedral's domed gallery was noted for its remarkable ability to propagate a whisper around its circumference with little apparent diminishment in the sound intensity. Effectively, sound seemed to "cling" to the circular walls of the structure where the effect appeared to be strongest. Using a candle flame as an acoustic sensor, Rayleigh revealed that the sound waves were indeed confined very close to the cathedral wall, with negligible intensity in the center. Rayleigh realized that the phenomenon must be at least in part related to the waveguiding and resonance effects due to sound reflecting at shallow angles from the gallery wall and the associated resonance. He was the first to use the recently-discovered Bessel equations to describe the resonances [79, 80], although he lacked the computational resources needed to solve the higher-order cases exactly.

Similar to the way in which sound travels in a whispering gallery such as St. Paul's cathedral (or astronomical observatory domes, where they are commonly the source of much entertainment), light waves can also be confined to form similar types of circular resonances.

9
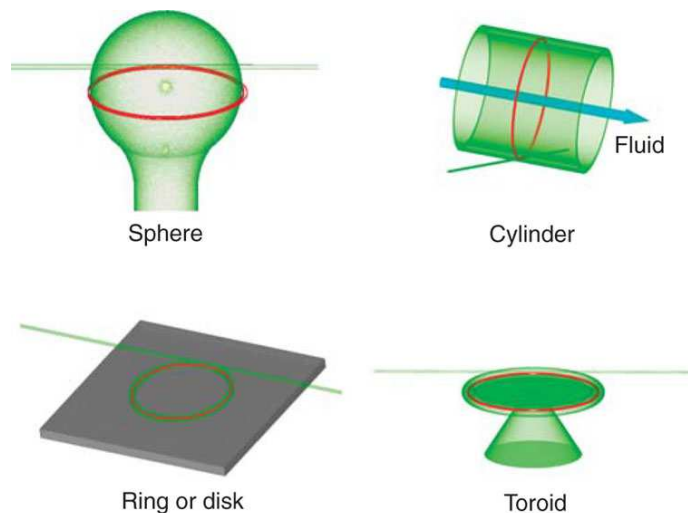
Figure 1.4: Some common circular geometries that support WGMs. The location of the WGMs are highlighted in red. The blue arrow is the flow of the analyte through a capillary. Figure from Ref. [6].

Light trapped in a transparent circular dielectric structure can propagate around the circumference by total internal reflection, building up the optical version of a whispering gallery mode. For light, the analogue of St. Paul's cathedral is a dielectric microsphere inside which light can propagate by total internal reflection. The ratio of microsphere size to the optical wavelength is similar to the size of St. Paul's cathedral with respect to typical acoustic wavelengths. Thus, the term "whispering gallery mode" is now commonly used to describe spherical or circular electromagnetic resonances as well as acoustic ones. A variety of structures support optical WGMs, including microspheres [81, 82, 83], toroids [84], microdisks [85], capillaries [86, 87, 88], and fibers [71, 89, 90] (Fig. 1.4).

1.3 A brief derivation of whispering gallery modes

This thesis focuses on three sensor geometries that can support WGMs: the dielectric microsphere, the cylindrical fiber, and the hollow cylindrical microcapillary. These structures will be coated with a layer of silicon quantum dots embedded in an oxide matrix. A fraction of the QD fluorescence is emitted into the WGMs of the resonator. A brief mathematical description of the WGMs is therefore of importance in order to understand how these structures can act as refractometric or biosensors.
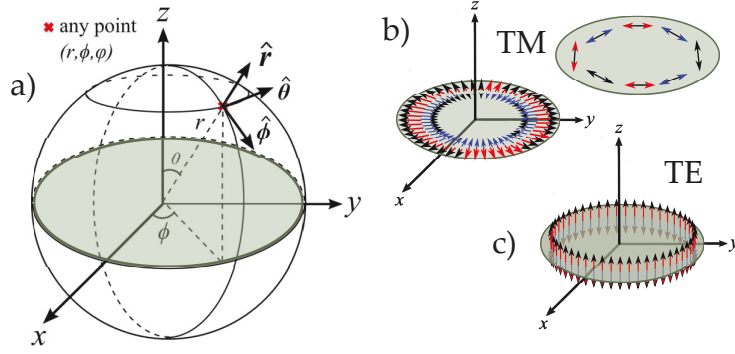
Figure 1.5: (a) Spherical coordinate system used in this work. (b) The electric field directions associated with the TE and TM polarizations. The coloured arrows indicate the electric field direction. Adapted from Ref. [7]

The mode numbers n, m, and l are generally used to specify any particular WGM. The radial mode number n represents the number of electric field intensity maxima along the radial direction (*i.e.* from the center to the edge of the structure). The "angular" number l is related to the angular momentum of the photon that circulates in the cavity, given by $L \approx ap = a\hbar k = 2\pi a\hbar N/\lambda = \hbar l$ where a is the radius of the cavity and p is the linear momentum. The "azimuthal" mode number m, together with the angular number l, specify the number of electric field intensity maxima in both the azimuthal and polar directions of a dielectric sphere. The azimuthal number is restricted to $-l \leq m \leq l$. All modes have m wavelengths that fit around the sphere equator (*i.e.* there are $2m$ field intensity maxima), and $l - m + 1$ field intensity maxima in the polar direction. The sign of m designates the WGM propagation direction: clockwise or counterclockwise. For perfect spherical symmetry, all m are degenerate for a given l. In an equatorial mode (which in a cylinder is the only WGM with no axial component), $l = m$ implying l wavelengths along the equator and $l - m + 1 = 1$ polar maximum. The mode numbers can be used to calculate the spatial profiles of the electromagnetic field in these structures.

Additionally, electromagnetic WGMs have two polarizations. In this work, they will be defined with respect to the WGM plane of propagation. Thus, the TE polarization has the E-field perpendicular to the equatorial plane of a microsphere, or parallel to the axis of a cylinder. The TM polarization has the H-field in these directions (so the E-field is either radial or tangential with respect to the WGM plane (Fig. 1.5)).

A simple mathematical description of the WGMs typically starts from the Helmholtz equation, given by:

$$\nabla^2 \mathbf{E} + k^2 n_i^2 \mathbf{E} = 0, \qquad (1.1)$$

or equivalently,

$$\nabla \times \nabla \times \mathbf{E} - k^2 n^2 \mathbf{E} = 0, \qquad (1.2)$$

where k is the vacuum wavevector and n_i is the refractive index. The Helmholtz equation follows from Maxwell's equations with the assumption that the electric field has a simple "harmonic" time dependence given by

$$\mathbf{E} = \mathbf{E_0}\, e^{-i\omega t}. \qquad (1.3)$$

The solutions to the Helmholtz equation are "harmonic" in frequency or time. A "harmonic" function is a mathematical term for a function $u(x, y)$ that has continuous second-order partial derivatives and satisfies $\nabla^2 u(x, y) = 0$ [91]. Harmonic solutions to the Helmholtz equation can represent the spatial or temporal behaviour of electromagnetic waves. They can be used to model the resonant frequencies of a given waveguide, and simulate how the field evolves over time. In order to calculate characteristics of a WGM-type optical sensor (*e.g.* the sensitivity and resonant wavelength), the Helmholtz equation is solved with the appropriate boundary conditions. The derivation of the harmonic solutions and the accompanying boundary problems will be shown first with a microsphere, and then with the cylindrical geometries.

1.3.1   WGM in a coated microsphere

In order to model the resonances of a microsphere, the Helmholtz equation will be solved in the spherical coordinate system. In this system, the Helmholtz equation is represented by

$$\frac{1}{r^2}\frac{\partial}{\partial r}(r^2\frac{\partial \mathbf{E}}{\partial r^2}) + \frac{1}{r^2 sin\theta}\frac{\partial}{\partial \theta}(sin\theta\frac{\partial \mathbf{E}}{\partial \theta}) + \frac{1}{r^2 sin^2\theta}\frac{\partial^2 \mathbf{E}}{\partial \phi^2} + (k_0 n_i)^2\mathbf{E} = 0, \qquad (1.4)$$

where k_0 is the resonant wave number, n_i is the refractive index, and the spherical coordinates are given by the radial direction r, the polar direction θ, and the azimuthal direction ϕ (Fig. 1.5).

Through the method of separation of variables, spherical wave functions represent the particular solutions of this equation. This method assumes equation 1.4 is separable, such that the solution can be written as a product of independent functions $R(r), \Theta(\theta)$, and $\Phi(\phi)$ which only depend on r, θ, or ϕ respectively. Accordingly,

$$\mathbf{E}(r, \theta, \phi) = R(r) \Theta(\theta) \Phi(\phi). \tag{1.5}$$

The goal here is to "separate" the solution to Eq. 1.4 into independent equations for each variable. These independent equations represent the electric field distributions in each coordinate. After substituting Eq. 1.5 into Eq. 1.4, one obtains

$$\frac{sin^2\theta}{R}\frac{d}{dr}(r^2\frac{dR}{dr}) + \frac{sin\theta}{\Theta}\frac{d}{d\theta}(sin\theta\frac{d\Theta}{d\theta}) + \frac{1}{\Phi}\frac{d^2\Phi}{d\phi^2} + (k_0 n_i)^2 r^2 sin^2\theta = 0. \tag{1.6}$$

Here the azimuthal angle ϕ only appears in the third term. Again, the left hand side must be zero therefore each term must be a constant because the terms depend on different independent variables. To start, one sets the third term equal to an arbitrary constant written for later convenience as $-m^2$:

$$\frac{1}{\Phi}\frac{d^2\Phi}{d\phi^2} = -m^2. \tag{1.7}$$

and through some rearranging, one obtains a differential equation for the azimuthal coordinate:

$$\frac{d^2\Phi}{d\phi^2} + m^2\Phi = 0. \tag{1.8}$$

This equation has a well known solution that describes how the electric field is distributed in the azimuthal direction:

$$\Phi(\phi) = a_m \, cos(m\phi) + b_m \, sin(m\phi), \tag{1.9}$$

where a_m and b_m are proportionality constants. Spherical symmetry requires that $\Phi(\phi) = \Phi(\phi + 2\pi)$ therefore m is an integer. Substituting $\Phi(\phi)$ back into 1.6, one obtains

$$\frac{1}{R}\frac{d}{dr}(r^2\frac{dR}{dr}) + \frac{1}{\Theta\sin\theta}\frac{d}{d\theta}(\sin\theta\frac{d\Theta}{d\theta}) + k^2 n_i^2 - \frac{m^2}{\sin^2\theta} = 0. \tag{1.10}$$

Now, the first term only depends on r, and second and last terms on θ. Then 1.10 can be similarly separated into two independent equations:

$$\frac{1}{R}\frac{d}{dr}(r^2\frac{dR}{dr}) + k^2 r^2 = l(l+1), \tag{1.11}$$

and

$$\frac{1}{\Theta\sin\theta}\frac{d}{d\theta}(\sin\theta\frac{d\Theta}{d\theta}) - \frac{m^2}{\sin^2\theta} = -l(l+1), \tag{1.12}$$

where $l(l+1)$ is another arbitrary constant. These equations can also be written in a more standard form:

$$\frac{d}{dr}(r^2\frac{dR}{dr}) + [k^2 r^2 - l(l+1)]R = 0, \tag{1.13}$$

and

$$\frac{1}{\sin\theta}\frac{d}{d\theta}(\sin\theta\frac{d\Theta}{d\theta}) + [l(l+1) - \frac{m^2}{\sin^2\theta}]\Theta = 0 \tag{1.14}$$

respectively. Together the equations 1.13 and 1.14 represent the radial and angular distributions of a spherical WGM corresponding to a given m and l, so they must be solved simultaneously in order to obtain the electric field profile.

The radial electric field distribution $R(r)$ can be written as the general solution of equation 1.13. This equation is known as the spherical Bessel equation. Its two linearly independent solutions are the lth-order spherical Bessel functions of the first and second kind, denoted as $j_l(n_i k_9 r)$ and $y_l(n_i k_0 r)$ respectively. The general solution can be written as a linear combination of the two solutions:

$$R(r) = c_l j_l(n_i k_0 r) + d_l y_l(n_i k_0 r) \tag{1.15}$$

where c_l and d_l are proportionality constants. The radial coordinate $R(r)$ in a microsphere is constrained by the fact that the electric field in the center of the sphere is finite. Spherical Bessel functions have the properties:

$$j_l(n_ik_0r) \rightarrow \text{finite}, \qquad \text{when } n_ik_0r \rightarrow 0,$$

$$y_l(n_ik_0r) \rightarrow \infty, \qquad \text{when } n_ik_0r \rightarrow 0. \tag{1.16}$$

For a finite function at $r \rightarrow 0$, $y_l(n_ik_0r)$ should be suppressed, therefore $d_l = 0$.

The $R(r)$ field function is modeled by another solution set: the spherical Hankel functions of the first and second kind. These are linear combinations of Bessel functions:

$$h_l^{(1)}(n_ik_0r) = j_l(n_ik_0r) + i\, y_l(n_ik_0r) \tag{1.17}$$

$$h_l^{(2)}(n_ik_0r) = j_l(n_ik_0r) - i\, y_l(n_ik_0r) \tag{1.18}$$

For a microsphere with a diameter much larger than the wavelength, the approximation $n_ik_0r/l \gg 1$ can be made. Then an asymptotic expansion of the spherical Hankel functions is consistent with two spherical waves propagating in opposite directions: a spherical wave traveling outward in the positive r direction,

$$h_l^{(1)}(n_ik_0r) \approx \frac{1}{n_ik_0r}e^{i\,(n_ik_0r-l\pi/2-\pi/2)} \tag{1.19}$$

and a wave traveling inward to the center,

$$h_l^{(1)}(n_ik_0r) \approx \frac{1}{n_ik_0r}e^{-i\,(n_ik_0r-l\pi/2-\pi/2)} \tag{1.20}$$

Finally, the time evolution of the resonance can be obtained by multiplying equations 1.19 and 1.20 with e^{-ickt} (Eq. 1.3) .

Similarly, we can also solve Eq. 1.14 for the electric field distribution in the polar direction. Eq. 1.14 is known as the Legendre equation, with a general solution given by:

$$\Theta(\theta) = e_{lm}P_l^m(\cos\theta) + f_{lm}Q_l^m(\cos\theta) \tag{1.21}$$

where $P_l^m(\cos\theta)$ and $Q_l^m(\cos\theta)$ are the associated Legendre polynomials, which are the linearly independent solutions to the Legendre equation. The variables e_{lm} and f_{lm} are arbitrary constants.

15

The field is finite everywhere, so the next task is to constrain Eq. 1.21, the general solution to Eq. 1.14, to be finite. $P_l^m(\cos\theta)$ is finite for integer l when $0 \leq \theta \leq \pi$, and infinite for non-integer l. Therefore angular mode number l must be an integer. The azimuthal mode number m takes values from $-l$ to l, and thus is also an integer.

On the other hand, $Q_l^m(\cos\theta) \to \infty$ when $0 \leq \theta \leq \pi$. The domain of the polar direction Θ is $0 \leq \theta \leq \pi$ from spherical coordinates, which is the same domain as Q_l^m, so one sets $f_l^m = 0$ to eliminate Q_l^m. The solution for Eq. 1.14 is then

$$\Theta(\theta) = e_{lm}P_l^m(\cos\theta). \tag{1.22}$$

Thus the electric field structure of a spherical WGM is fully described: the radial portion of the field is described by Eqs. 1.19 and 1.20, and the polar portion by Eq. 1.22. This is the standard derivation than can also be found in many texts and review papers on WGMs. From here on, however, we will only be concerned with the radial field profiles. This is because the equatorial WGMs are the strongest (*i.e.* they have the highest Q-factor) in microspheres and because the equatorial WGMs are the only non-propagating modes of significance in the cylindrical structures investigated in this thesis.

Now that we have the general solutions to the Helmholtz equation (Eq. 1.4), we can apply boundary conditions to model the field profile in the radial direction. The radial field functions depend on the refractive index profile of the structure in question. For a bare microsphere, the refractive index profile is a piecewise function with refractive index n_1 in the center out to radius b, and the surrounding medium of refractive index n_2. For a layered cylinder, we have a third index n_3 (Fig. 1.6).

The radial field function can be written in terms of Riccati-Bessel functions in each domain. Riccati-Bessel functions are used here instead of standard Bessel functions because when their square is plotted with respect to the radial direction, the resulting function scales like electromagnetic energy density in a spherical cavity [92].

In this thesis, a high-index QD layer will be deposited on the microsphere. A coating of differing refractive index on the surface of the sphere adds a "layer of complexity" to the derivation. However, the resonance solutions are generally similar to that of an uncoated sphere [93]. For a coating of thickness $t \equiv a - b$ (Fig. 1.6) on a sphere with radius b, the

radial profile of the refractive indices can be written as [94]:

$$n(r) = \begin{cases} n_1 & r < b \\ n_2 & b < r < a \\ n_3 & r > a \end{cases} \qquad (1.23)$$
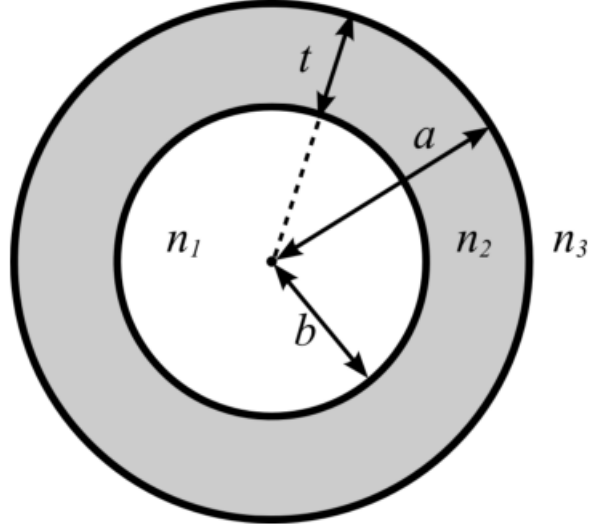
Figure 1.6: Schematic of a 3-layer structure of a coated microsphere, from Ref. [7]

This is a 3-layer problem: layer 1 is a glass microsphere with radius $a - t$ and refractive index n_1, layer 2 is a coating with thickness t and refractive index n_2, and layer 3 is the outside medium of refractive index n_3. Since we are interested in the radial field, we can define $S(r)$ and $T(r)$ to model the electric field functions of the TE and TM polarizations respectively [95, 94, 93]. The TE polarization has the field perpendicular to the equatorial plane of the sphere (Fig. 1.5), and the field function $S_l(r)$ can be written as

$$S_l(r, k) = \begin{cases} A_l \Psi_l(n_1 k_0 r) & r < b \\ B_l \xi_l^{(2)}(n_2 k_0 r) + C_l \xi_l^{(1)}(n_2 k_0 r) & b \leq r \leq a \\ D_l \xi_l^{(1)}(n_3 k_0 r) & r > a \end{cases} \qquad (1.24)$$

where A_l, B_l, C_l and D_l are proportionality constants. $\Psi = n_i k_0 r \cdot j_l(n_i k_0 r)$ is the lth-Riccati-Bessel function. The Riccati-Hankel functions of the first and second kind are $\xi_l^{(1)} = n_i k_0 r \cdot [j_l(n_i k_0 r) + i y_l(n_i k_0 r)]$ and $\xi_l^{(2)} = n_i k_0 r \cdot [j_l(n_i k_0 r) - i y_l(n_i k_0 r)]$ respectively.

Next, Maxwell's equations state that the electric field and its derivative must be continuous for the TE polarization. At boundary $r = b$, $A_l \Psi_l(n_1 k_0 r)$ must equal $B_l \xi_l^{(2)}(n_2 k_0 r) +$

17

$C_l \xi_l^{(1)}(n_2 k_0 r)$ and their derivatives must be equal; the functions at boundary $r = a$ must meet similar conditions [96]. The set of equations obtained from these equalities can be written as a ratio:

$$\frac{n_2 \xi_l^{(1)}(n_3 k_0 a)}{n_3 \xi_l^{'(1)}(n_3 k_0 a)} = \frac{B_l/C_l \xi_l^{(2)}(n_2 k_0 a) + \xi_l^{(1)}(n_2 k_0 a)}{B_l/C_l \xi_l^{'(2)}(n_2 k_0 a) + \xi_l^{'(1)}(n_2 k_0 a)}, \tag{1.25}$$

where

$$\frac{B_l}{C_l} = \frac{-n_1 \psi_l'(n_1 k_0 a)\xi_l^{(1)}(n_2 k a) + n_2 \xi_l^{'(1)}(n_2 k_0 a)\psi_l(n_1 k_0 a)}{-n_2 \xi_l^{'(2)}(n_2 k_0 a)\psi_l(n_1 k_0 a) + n_1 \psi_l'(n_1 k_0 a)\xi_l^{(2)}(n_2 k_0 a)}. \tag{1.26}$$

The resonance wave vectors can be obtained by numerically solving for the roots k_0 of this equation. For any given solution, the resonant wavelength is $\lambda_0 = \frac{2\pi}{\mathrm{Re}[k_0]}$ and the Q-factor is given by [28]

$$Q = \frac{\mathrm{Re}[k_0]}{2\mathrm{Im}[k_0]}. \tag{1.27}$$

In the case of the TM polarization, the radial field profile is [92]:

$$T_l(r, k) = \begin{cases} a_l \Psi_l(n_1 k_0 r) & r < b \\ b_l \xi_l^{(2)}(n_2 k_0 r) + c_l \xi(n_2 k_0 r) & b \leq r \leq a \\ d_l \xi_l^{(1)}(n_3 k_0 r) & r > a \end{cases}. \tag{1.28}$$

The boundary conditions are different in this case, leading to a slightly different set of equalities:

$$\frac{n_3 \xi_l^{'(1)}(n_3 k_0 a)}{n_2 \xi_l^{(1)}(n_3 k_0 a)} = \frac{b_l/c_l \xi_l^{(2)}(n_2 k_0 a) + \xi_l^{'(1)}(n_2 k_0 a)}{b_l/c_l \xi_l^{'(2)}(n_2 k_0 a) + \xi_l^{(1)}(n_2 k_0 a)}, \tag{1.29}$$

with

$$\frac{b_l}{c_l} = \frac{-n_2 \xi_l^{(1)}(n_2 k_0 a)\psi_l'(n_1 k_0 a) + n_1 \psi_l(n_1 k_0 a)\xi_l^{'(1)}(n_1 k_0 a)}{-n_1 \psi_l(n_1 k_0 a)\xi_l^{'(2)}(n_2 k_0 a) + n_2 \xi_l^{(2)}(n_2 k_0 a)\psi_l'(n_1 k_0 a)}. \tag{1.30}$$

1.3.2 From spherical to cylindrical whispering gallery modes

Microcavities with cylindrical geometries that support WGMs will also be used in this work. There are two cylindrical geometries that will be discussed: glass capillaries and optical fibers. In order to obtain the WGM field structure, the method is very similar to that of a coated microsphere. It is again a 3-layer problem. The fiber has a coating of thickness $t \equiv a - b$, where a is the radius of the bare fiber, and b is the outer radius including the coating. The radial profile of the refractive indices can be written as a piecewise function equivalent to that of the coated microsphere.

For a solid cylindrical dielectric waveguide *i.e.* an optical fiber, the Helmholtz equation can be solved in the cylindrical coordinate system using separation of variables. This leads again to the radial profile in Eq. 1.24, where now b is the radius of the fiber, and t is again the thickness of the coating on the fiber. For a capillary geometry, the coating is on the inner surface and the analyte runs through the core. The film thickness is always $t = a - b$, so here a is the inner radius of the bare capillary channel and b is the inner radius after the coating is applied.

By a mathematically similar process to the spherical WGM derivation, there are two polarizations whose field functions simply use cylindrical Bessel functions instead of Riccati-Bessel ones [86] :

$$
S_l(r,k) = \begin{cases} A_l \Psi_l(n_1 k_0 r) & r < b \\ B_l \xi_l^{(2)}(n_2 k_0 r) + C_l \xi_l^{(1)}(n_2 k_0 r) & b \leq r \leq a \\ D_l \xi_l^{(1)}(n_3 k_0 r) & r > a \end{cases} \tag{1.31}
$$

and

$$
T_l(r,k) = \begin{cases} a J_l(n_1 k_0 r) & r \leq a - t \\ b_l H_l^{(2)}(n_2 k_0 r) + c_l H_l^{(1)}(n_2 k_0 r) & a - t < r \leq a \\ d_l H_l^{(1)}(n_3 k_0 r) & r > a \end{cases} \tag{1.32}
$$

where $J_l(n_1 k_0 r)$ is the lth order cylindrical Bessel function of the first kind. $H_l^{(1)}(n_2 k_0 r)$, $H_l^{(2)}(n_2 k_0 r)$ are the cylindrical Hankel functions of the lth order, and (1) or (2) indicates the first or second kind respectively.

The radial field corresponding to each polarization in a cylindrical geometry can also be found by solving the radial field Eq. 1.24 with boundary conditions, as with the spherical WGMs. For the TE polarization, the solution is [86]:

$$
\frac{n_3 H_l^{(1)'}(n_3 k_0 a)}{n_2 H_l^{(1)}(n_3 k_0 a)} = \frac{B_l/C_l H_l^{(2)'}(n_2 k_0 a) + H_l^{(1)'}(n_2 k_0 a)}{B_l/C_l H_l^{(2)}(n_2 k_0 a) + H_l^{(1)}(n_2 k_0 a)}, \tag{1.33}
$$

where

$$
\frac{B_l}{C_l} = \frac{n_2 J_l(n_1 k_0 b) H_l^{(1)'}(n_2 k_0 b) - n_1 J_l'(n_1 k_0 b) H_l^{(1)}(n_2 k_0 b)}{-n_2 J_l(n_1 k_0 b) H_l^{(2)'}(n_2 k_0 b) + n_1 J_l'(n_1 k_0 b) H_l^{(2)}(n_2 k_0 b)}. \tag{1.34}
$$

Similarly the TM polarization is given by:

$$\frac{n_2 H_l^{(1)'}(n_3 k_0 a)}{n_3 H_l^{(1)}(n_3 k_0 a)} = \frac{b_l/c_l H_l^{(2)'}(n_2 k_0 a) + H_l^{(1)'}(n_2 k_0 a)}{b_l/c_l H_l^{(2)}(n_2 k_0 a) + H_l^{(1)}(n_2 k_0 a)}, \tag{1.35}$$

where

$$\frac{b_l}{c_l} = \frac{n_1 J_l(n_1 k_0 b) H_l^{(1)'}(n_2 k_0 b) - n_2 J_l'(n_1 k_0 b) H_l^{(1)}(n_2 k_0 b)}{-n_1 J_l(n_1 k_0 b) H_l^{(2)'}(n_2 k_0 b) + n_2 J_l'(n_1 k_0 b) H_l^{(2)}(n_2 k_0 b)}. \tag{1.36}$$

By solving for the roots k_0, similarly to the sphere, one can obtain the radial mode orders corresponding to the complex wavevectors k_{0_1}, k_{0_2}, etc.

1.4   Basic properties of whispering gallery modes

The previous mathematical description of the whispering gallery modes helps to put into context some of the basic parameters that are used to describe their characteristics as they appear in a fluorescence spectrum. The quality factor, free spectral range (to be described below) and many other parameters can be calculated directly using Eqs. 1.3.25-1.3.36. These parameters are typically measured via an analysis of the WGM mode spectrum, and are important characteristics from the point of view of sensing applications. Thus, a brief description of the key physical parameters associated with a WGM spectrum will be provided here.

1.4.1   Quality factor

One important parameter used to characterize a microresonator is its quality factor. This describes the rate at which electromagnetic energy is lost from a microresonator cavity. The definition of the Q factor with respect to the stored energy is:

$$Q = 2\pi \frac{energy\ stored}{energy\ dissipated\ per\ optical\ cycle} \tag{1.37}$$

Equivalently for moderate to high Q-factors, Eq. 1.37 can be related to the width of the resonance [59]:

$$Q = \frac{f_0}{\Delta f} = \frac{\lambda_0}{\Delta \lambda} = \frac{\omega_0}{\Delta \omega} \tag{1.38}$$

where f_0, λ_0, and ω_0 are the resonant frequency, resonant wavelength, and resonant angular frequency of the cavity respectively, and Δf, $\Delta \lambda$, and $\Delta \omega$ are the full-width half maximum (FWHM) in their respective units. Thus, a smaller linewidth implies a higher Q-factor. From Eq. 1.38 the characteristic $1/e$ decay time for photons in the cavity is $\tau = Q/\omega_0$ [97] where ω_0 is the angular frequency of the electromagnetic oscillation in the cavity. In optical microcavities, the highest Q-factors ever reported are $\sim 10^{10}$ at a wavelength of 633 nm in a silica microsphere [98], at which the absorption of the glass is minimal. In contrast, the Q-factors observed in fluorescence WGM spectra are typically much lower (i.e., $Q \approx 10^2 - 10^3$) [87, 62]. This is often a result of scattering or absorption losses present in the fluorescent material used in the cavity. Therefore, a more detailed discussion of the loss mechanisms and their effect on the cavity Q factor is warranted.

1.4.1.1 Loss mechanisms

The Q-factor associated with any microresonator is ultimately limited by at least one of several possible loss mechanisms. These can be categorized into radiative losses, scattering losses due to surface roughness, and absorption losses. Whichever mechanism dominates depends on the size and the material properties of the cavity. One can write an expression for the overall observable Q-factor for all loss mechanisms acting in parallel. Accordingly, [99]:

$$Q_{tot}^{-1} = Q_{rad}^{-1} + Q_{scat}^{-1} + Q_{abs}^{-1} + \sum_i Q_i^{-1}. \tag{1.39}$$

Each of the Q-factors contributing to Q_{tot} (the total Q-factor) will be briefly discussed below. Q_{rad} is the Q-factor limited by radiative loss *(i.e.* photons escaping due to surface curvature). Radiative loss occurs in cavities with curved surfaces because the electric field at the boundary extends out to infinity, instead of being truly evanescent. Smaller spherical or cylindrical cavities have larger Q_{rad} because their surface curvature is sharper.

Q_{scat} is the limiting Q-factor due to light scattering. Surface roughness is a dominant scattering related loss mechanism in large silica microspheres [7] and lithographically fabricated microdisks. Previous work calculated that in microdisks larger than 4 μm in diameter, Mie scattering from the quantum dots is an insignificant loss mechanism compared to Q_{scat}

and Q_{abs} [100]. The microspheres in this work are much larger than 4 μm, therefore Mie scattering is probably not a loss mechanism for the structures in this work.

Q_{abs} is the limiting Q-factor associated with material absorption. In the SiQD-coated silica microspheres used in this work, band-to-band or intraband absorption can occur in the SiQDs [101]. Absorption-related losses and scattering losses have been shown to be comparable in SiQD-coated microdisks [101] and microspheres [7].

1.4.2 Free spectral range

The free spectral range (FSR) is the frequency or wavelength separation between two adjacent resonances having the same radial (n) and azimuthal (m) quantum numbers, but differing by one angular (l) number. The FSR can be approximated very roughly for a sphere according to [102]:

$$\Delta f_{FSR} = f_{n,m,l} - f_{n,m,(l-1)} \approx \frac{c}{2\pi a} \frac{arctan[\sqrt{n_i^2 - 1}]}{\sqrt{n_i^2 - 1}} \qquad (1.40)$$

where $f_{n,m,l}$ and $f_{n,m,l-1}$ are the resonant frequencies of the adjacent modes specified by (n, m, l) and $(n, m, l - 1)$ respectively, c is the speed of light in vacuum, a is the radius of the cavity, and n_i is its index of refraction. The free spectral range can be a measure of the spectral resolution of a sensor. Experimentally, a small FSR indicates that the modes may be difficult to resolve and may even overlap. For sensors that rely on wavelength shifts as the measurement mechanism, the FSR may limit the sensing range because of the periodicity of the phase.

1.4.3 Finesse

The finesse is a figure of merit closely related to Q-factor and the FSR. Finesse is the ratio of the free spectral range to the full width half maximum of the resonance peak. It is therefore is a measure of the spectral resolution of the cavity [103]. Physically, the finesse is equal to the number of round trips a photon takes in a cavity before it is lost. The finesse can also be defined in relation to the Q-factor, according to:

$$\mathcal{F} = \frac{\Delta f_{FSR}}{\Delta f} = Q \frac{\Delta f_{FSR}}{f_0}. \qquad (1.41)$$

1.4.4 WGM visibility

The visibility is a figure of merit that describes the contrast of WGM features against the background signal. A high visibility means that the interference maxima (*i.e.* the WGMs in the present work) are relatively easily distinguished from the background fluorescence. The visibility (V_I) takes the usual definition:

$$V_I = \frac{I_{max} - I_{min}}{I_{max} + I_{min}}. \tag{1.42}$$

where I_{max} is the peak intensity of a mode and I_{min} is the minimum intensity between adjacent modes.

1.4.5 Mode volume

The mode volume (V_m) describes the spatial confinement of energy in the cavity. In other words, it is a description of the physical "size" of the mode. Mathematically, the mode volume is defined as the normalized volume integral of the electromagnetic energy in the cavity. For a spherical resonator one can therefore write:

$$V_m = \frac{\int_V \epsilon(\mathbf{r}) \mid \mathbf{E}(\mathbf{r}) \mid^2 d^3\mathbf{r}}{max[\epsilon(\mathbf{r}) \mid \mathbf{E}(\mathbf{r}) \mid^2]}. \tag{1.43}$$

Here $\epsilon(\mathbf{r})$ is the dielectric permittivity along the radial direction, $\mid \mathbf{E}(\mathbf{r}) \mid^2$ is the squared electric field amplitude, and the variable of integration is $\mathbf{r}$.

For a microsphere, the integral in Eq. 1.43 is divergent. In other words, because the cavity is lossy, the energy extends outward to infinity. This is the so-called "open-resonator problem" and means that in practice the integral is generally taken over some arbirary limit of integration. For example, one might assume that by 100$\mathbf{r}$ (*i.e.* 100 times the radius of a microsphere [104]) the energy has decreased to the point that we can effectively call the intensity zero. For this reason, the term "effective" mode volume is sometimes used to describe Eq. 1.43.

Along with Q-factor, the mode volume is a parameter that affects the interaction of an emitter (*e.g.* an atom or a quantum dot) with the WGM. Large Q-factors and small mode volumes increase the coupling strength of the interaction; in other words, an emitter can

be said to be better-coupled to a cavity when the ratio Q/V_m is high. A high Q/V_m can strongly affect the decay rate of the emitter, for example, through the so-called Purcell effect (to be described in Section 1.5). Microsphere cavities can have high Q-factors but the mode volumes are also fairly large, in the range of hundreds of cubic wavelengths. Photonic crystal and micropillar-type cavities have smaller Q-factors (up to a few tens of thousands) but the mode volume can be as small as a few cubic wavelengths, giving these cavities among the highest Q/V_m ratios so far obtained [105].

1.5 Cavity-emitter interactions

Whispering gallery modes *can* enhance or suppress the emission rates of QDs, depending on whether the QD emission frequency corresponds to a WGM resonance or not. Therefore, an investigation of quantum dot ensembles coupled to a cavity might show differences in the ensemble luminescence dynamics as compared to those observed for "uncoupled" QDs.

1.5.1 Basic introduction

An emitter that is resonant with a cavity is said to be "strongly" or "weakly" coupled to the cavity [59, 97]. When an emitter such as an atom or quantum dot emits into a cavity via radiative decay, the emitted photons can be trapped for a time in the cavity. These "resonant photons" can eventually be lost due to the finite Q-factor of the cavity, or they can be reabsorbed by the emitter. The coupling regime depends on whether cavity loss or re-absorption is more likely to occur.

There are three key rates that determine whether the emitter-cavity interaction is strongly or weakly coupled [97, 59]. First, the coupling rate g_0 is a measure of the rate at which the emitter exchanges photons with the field. Second, the cavity loss rate κ measures the rate at which photons are lost from the cavity. The cavity loss rate is an intrinsic cavity parameter that depends on the Q-factor, as given by $\kappa = \omega/Q$. This reflects that a high Q-factor cavity has a smaller loss rate. Third, the decay rate γ is the photon decay rate into non-cavity modes. The ratio of photons emitted into the cavity *vs.* those emitted into free space modes is given by $\beta = W_{cav}/(W_{cav}+W_{free})$. The emitter-cavity system is said to be strongly coupled if $g_0 > \{\kappa, \gamma\}$, whereas if $g_0 < \{\kappa, \gamma\}$, the system is said to be weakly

coupled.

Effectively, the strong coupling regime implies that re-absorption is faster than the characteristic time it takes to lose photons from the cavity [59, 97]. This means that the process of photon emission is reversible and coherent. Systems in cavity-quantum-electrodynamics investigations are generally said to be strongly coupled [106]. Achieving strong coupling usually requires ultra-high Q-factor, and often low temperatures ($< 10\,\mathrm{K}$) to limit the thermal decoherence [107, 108, 109, 110]. In the present work, the conditions for strong coupling will not be met and the SiQD-cavity system will be weakly coupled.

1.5.2 Weak coupling: the Purcell factor

In the weak coupling regime, the main effect is that the spontaneous emission rate of an emitter is modified as a result of the optical density of states in the cavity. The rate enhancement or suppression is quantified by the Purcell factor, F_p, which is simply the ratio of the emitter lifetime in the cavity compared to that in free space [59, 97, 111]. The general emission rate can be derived from Fermi's Golden Rule for spontaneous emission of a two-level atom into any available density of states [112]:

$$W_{general} = \frac{2\pi}{\hbar^2} \int_0^\infty |\langle f| H |i\rangle|^2 \rho(\omega)\Lambda(\omega)d\omega, \qquad (1.44)$$

where $\langle f| H |i\rangle$ is the matrix element for the atom-field transition, $\rho(\omega)$ is the density of states into which emission can occur, and $\Lambda(\omega)$ is the density of states of the atomic transition. For a quantum dot in a cavity mode, it is usually assumed that $\int_0^\infty \Lambda(\omega)d\omega = 1$ $i.e.$ the density of states of the QD (the emitter) is narrow (a δ-function) compared to the cavity mode [113]. In this case Fermi's Golden Rule can be written:

$$W_{cavity} = \frac{2\pi}{\hbar^2} |\langle f| H |i\rangle|^2 \rho(\omega), \qquad (1.45)$$

To derive the idealized cavity-enhanced emission rate, the following three simplifying assumptions can be made [59, 97, 112]:

- The QD can be modeled as a dipole that is polarization matched with the field in the cavity.

- The QD resonance is exactly in tune with a cavity resonance.

- The QD emission has an infinitesimal linewidth as discussed above.

With these assumptions, Eq. 1.5.2 has the following solution [97, 112]:

$$W_{cavity} = 4(\frac{d}{\hbar})^2 \frac{\hbar\omega}{2\epsilon_0 V_m} \frac{Q}{\omega},$$ (1.46)

where $d/\hbar$ is the dipole moment, V_m is the mode volume, ϵ_0 is the electric permittivity of free space, and Q is the cavity quality factor. Maximizing W_{cav} is a matter of increasing Q/ω or decreasing V_m with a given choice of emitter [114]. Dividing Eq. 1.46 by the free space emission rate [112]:

$$W_{free} = (\frac{d}{\hbar})^2 \frac{\hbar\omega^3}{\epsilon_0 \pi c^3},$$

where c is the speed of light, one obtains an idealized formulation of the Purcell factor. The Purcell factor is commonly written[‡] [97, 59, 111]:

$$F_p = \frac{W_{cavity}}{W_{free}} = \frac{3Q(\lambda/n_i)^3}{4\pi^2 V_m}.$$ (1.47)

where λ is the vacuum wavelength, and n_i is the refractive index. In real life, the assumptions 1-3 will not be met and the measured Purcell factor will be smaller than the idealized one represented by Eq. 1.47.

A brief summary of experimentally observed Purcell factors can be instructive. Ref. [114] reported a Purcell factor of 5 for InAs QDs embedded in GaAs/AlAs micropillars. A Purcell factor of 17 was recently reported with GaSb/GaAs QDs in a photonic crystal laser [115]. A single CdSe quantum dot coupled to a microsphere in Ref. [116] had a reported Purcell factor of 10. An ensemble of SiQDs in a Fabry-Perot cavity was shown to have an enhancement factor of 7 [117]. These values were all obtained by comparing the fluorescence decay lifetimes in the cavity as compared to that in free space. The relatively modest values suggest that the idealized Purcell factor represented by Eq. 1.47 significantly overestimates the actual Purcell enhancement for QD-cavity systems.

[‡]The factor of 3 is an averaging factor for the random electric dipole orientation to the vacuum field. It can be included in the density of states, as in Ref. [112], or more commonly in the matrix element as in Ref. [97, 59].

For QDs that are off-resonance, the observed Purcell factor will be less than unity (*i.e.* it will be fractional), indicating a suppression of the emission rate [113]. If the mode volume is estimated to be $V_m \sim (\lambda/2)^3$, then the idealized on-resonance Purcell factor is $\sim Q$ for QDs while it is only $\sim 1/Q$ for QDs that are off-resonance [112].

1.6   Sensing with whispering gallery modes

Although the QDs did not show any detectable Purcell effects in the ensemble emission dynamics, the structures investigated in the previous chapter may find sensor-type application on the basis of the luminescence spectra alone. In fact, whispering gallery mode devices have been developed as sensors capable of detecting single nanoparticles or molecular binding events [6, 118, 119]. This high level of sensitivity makes WGM sensors a powerful tool for label-free biosensing. This section defines the figures of merit that are often used to characterize WGM-based optical sensors in order to describe their sensing performance.

An important figure of merit is the refractometric sensitivity (S) of a sensor. The sensitivity is a measure of the magnitude of the sensor response to a change in the analyte. In the case of WGM sensors, the refractometric sensitivity is defined by the magnitude of the resonant wavelength shift in response to a change in the refractive index of the analyte:

$$S = \frac{d\lambda}{dn}. \tag{1.48}$$

The sensitivity is an intrinsic property of the sensor, and is independent of the measurement system.

The detection limit, or limit of detection (LoD), is the minimum *detectable* refractive index change. It is related both to the sensitivity and the "resolution" of the measurement system [120]:

$$LoD = \Delta n_{min} = \frac{\Delta \lambda_{min}}{S}. \tag{1.49}$$

$\Delta \lambda_{min}$ is the smallest detectable resonance wavelength change, which depends on factors such as the pitch (the ratio of the wavelength range to the number of pixels) of the measurement system and the signal-to-noise ratio. The resolution can be approximated as three
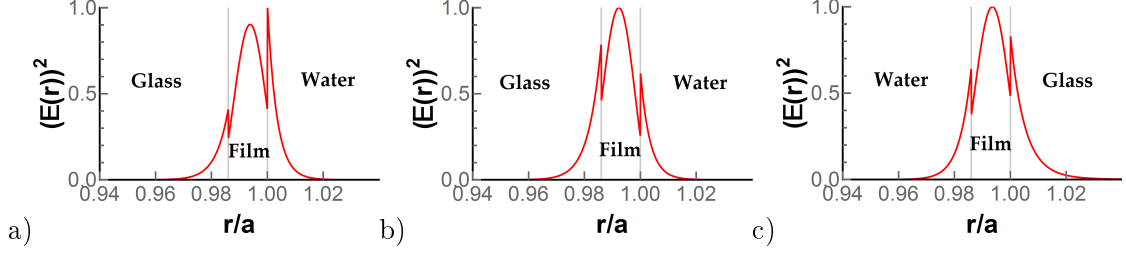
Figure 1.7: Calculated radial WGM field profiles for a) a coated microsphere, b) a coated fiber, and c) a coated microcapillary. For each, the WGM is mainly confined to the film and part of the mode samples the analyte, while part is in the glass. Shown is the TM polarization for $d = 50\mu$m, $l = 308$ and a coating thickness of $0.35\,\mu$m.

times the standard deviation (3σ) of the values of the WGM peaks under constant conditions.

In order to understand how to improve the sensitivity of WGM-based sensors covered in this work, the basic sensing mechanism must first be described. The WGM electric field is mostly confined within the cavity, with some of the mode extending into the analyte (Fig. 1.7). The "tail" of the field interacts with the analyte, so refractive index changes in the analyte affect the resonant wavelength of the WGM. This refractive index change can be either a bulk change in the analyte, or a local refractive index change caused by a molecule binding to the coating surface.

Knowing the radial profile of the WGM from Eqs. 1.24 and 1.32, one can estimate the refractometric sensitivity according to the methods derived by Teraoka and Arnold in three key references [93, 95, 121]. Accordingly, the sensitivity is related to the fraction of the WGM electric field energy in the analyte region. For the TE polarization, the intensities can be obtained by squaring Eq. 1.24 and integrating piecewise over the respective layers:

$$
\begin{aligned}
I_1 &\equiv \int_0^b A_l^2 [\Psi(n_1 k r_0)]^2 dr, \\
I_2 &\equiv \int_{a-t}^a [B_l \xi_l^{(2)}(n_2 k_0 r) + C_l \xi_l^{(1)}(n_2 k_0 r)]^2 dr, \text{ and} \\
I_3 &= \int_a^\infty [D_l \xi_l^{(1)}(n_3 k_0 r)]^2 dr,
\end{aligned}
$$

where the constants A_l, B_l, C_l, D_l, and k_0 are found for a microsphere from Eqs. 1.24, 1.25 and 1.26.

28

For the TM case, the situation is the same except that the constants A_l, B_l, C_l, and D_l are replaced by a_l, b_l, c_l, and d_l. An expression for the refractometric sensitivity of a microsphere with a high-index layer [119, 122] can then be defined for each polarization [94]. The TE sensitivity is given by:

$$S_{TE} = \frac{d\lambda}{dn} = \frac{\lambda}{n_3} \frac{n_3^2 I_3}{n_1^2 I_1 + n_2^2 I_2 + n_3^2 I_3}. \tag{1.50}$$

And for the TM case [93]:

$$S_{TM} = \frac{d\lambda}{dn_3} = \frac{k_0 a}{4n_3^2(I_1 + I_2 + I_3)} x_l^2 [-h_l^2(n_3 k_0 a) + (\frac{l(l+1)}{(n_3 k_0 a)^2} - 1)h_l^2(n_3 k_0 a) - \frac{h_l(n_3 k_0 a)\,h_l'(n_3 k_0 a)}{n_3 k_0 a}], \tag{1.51}$$

where $I_{1,2,3}$ is the energy density for the first, second, or third layer respectively, a is the radius of the microsphere, and $d\lambda$ is the change in resonant wavelength due to a refractive index change dn. The refractive indices n_1, n_2 are microsphere and coating respectively, while n_3 is the refractive index of the analyte. The term $h_l'(x)$ is the derivative with respect to x of the spherical Hankel function of the first kind. The constant m_l comes from the boundary value problem of Eq. 1.24:

$$x_l = \frac{n_2}{n_3} \frac{b_l h_l^{(2)}(n_2 k_0 a) + c_l h_l(n_2 k_0 a)}{h_l(n_3 k_0 a)}, \tag{1.52}$$

where $h_l^{(2)}$ is the spherical Hankel or Hankel function of the second kind. So the refractometric sensitivity depends on the refractive indices of the various media, the wavelength, and the size of the microsphere. For the sensitivity of a cylinder, Eq. 1.52 does not have a factor n_2/n_3.

1.6.1 Experimental considerations

Light can be coupled into WGM-based sensors via evanescent coupling or by integrating a fluorescent material into the cavity. Evanescent coupling is usually achieved by using a tapered fiber or waveguide [88, 105, 118, 123, 124, 125], prism [126], or surface grating coupler [65, 127] placed within the evanescent interaction length from the microsphere surface (typically less than 1 μm). Light from a tuneable laser is injected into the coupling device.

The position of the WGM wavelength peak is measured by scanning the wavelength of the tuneable laser and monitoring the transmission. Resonances then appear as dips in the transmission spectrum. This method has excellent wavelength shift resolution because the linewidth of the laser can be on the order of femtometers. One drawback of this scheme is that the coupling apparatus is often fragile and needs nanometer-motion precision.

Fluorescent coupling of light into WGMs is an alternative to evanescent coupling. This is achieved by embedding fluorophors such as quantum dots [7] or fluorescent polymers [128] into the cavity. The fluorescence overlaps with whispering gallery mode spectrum, which appears as a periodic array of sharp peaks in the fluorescence spectrum. The fluorophors can be excited by free space radiation and the photoluminescence scattered from WGMs is collected by an optical microscope and spectrometer. The main advantage of the fluorescence coupling scheme is that no fiber taper or other delicate positioning is needed. Another advantage is that the device is robust and easy to fabricate. One drawback is the low light levels compared to evanescent coupling and the correspondingly long collection times that may be needed to compensate for this [129].

Chapter 2

Experimental methods

2.1 Synthesis of silicon quantum dot films

The silicon quantum dot films studied in this thesis were formed by thermal dispropor-tionation of hydrogen silsesquioxane (HSQ; chemical formula $H_8Si_8O_{12}$) [8, 130]. The HSQ molecule has a cage-like structure (Fig. 2.1) consisting of $HSiO_3$ sub-units linked through shared oxygens. The HSQ solution used in this work is trademarked by the Dow Corning company as FOx-15, or "flowable oxide - 15". FOx-15 is composed of 15-30% by weight hydrogen silsequioxane dissolved in methyl isobutyl ketone (MIBK) to form a clear, slightly viscous solution.

The quantum dots were produced by a "dip-coating method". In this method, glass spheres, fibers, or capillaries were dipped into HSQ solution and were then annealed at high temperatures (1000°C or 1100°C) in an atmosphere of 5% H_2 + 95% N_2. The high temperature evaporates the solvent, evolves the excess hydrogen, and causes the HSQ cage structure to collapse and form a solid SiO_x film [8]. The film phase separates at high temperatures, leading to an ensemble of crystalline silicon nanoparticles embedded in an SiO_2-like matrix. The hydrogen in the annealing atmosphere helps to passivate the quantum dots, resulting in a brighter fluorescence [131].

There are many ways to fabricate SiQDs, among the most common being physical or chemical vapor deposition [132, 133] or ion implantation [134, 135]. However, the HSQ method has certain key advantages for the present work. Most importantly, it can be used to create non-planar QD films needed for coating various microcavity-type structures. The final coating is generally smooth and uniform. However, the stock HSQ solution needs to be
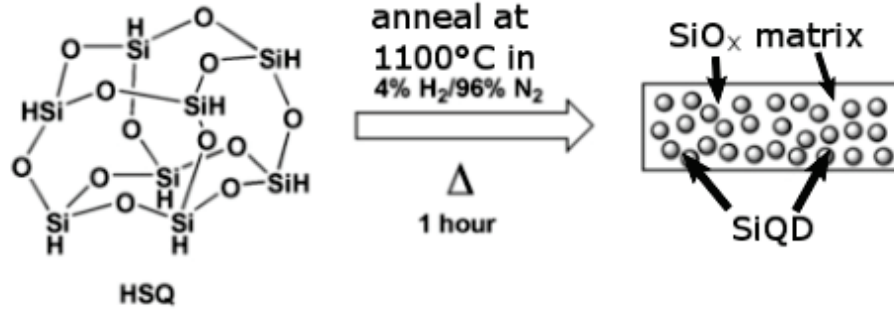
Figure 2.1: A schematic of the silicon quantum dot formation process. Adapted from Ref. [8].

stored in an inert atmosphere (glove box) and refrigerated below 4°C. Otherwise, the liquid solution gels quickly when exposed to air or moisture and becomes rapidly unusable. Vials of the FOx-15 starting solution must be transported from the inert atmosphere in the glove box and used immediately. Additionally, HSQ costs $\sim$ CA\$1000 for a 125 mL bottle; thus special care must be taken to avoid exposing the stock solution to atmosphere.

2.2 Preparation of QD-coated fibers, spheres, and capillaries

2.2.1 Fibers

First an $8 - 10$ cm length of single mode fiber was stripped of its jacket and buffer, and the resulting bare fiber was cleaned with denatured alcohol to remove debris. Then it was dipped to a depth of ~ 1 inch in a vial of HSQ for ~ 30 seconds. The fiber was immediately placed vertically in a custom-designed quartz crucible and annealed at 1100°C for one hour. The coating and annealing steps were repeated for up to three coatings in order to produce thicker films. During annealing, the fibers tended to bow slightly under their own weight and became brittle. (Fig. 2.2a)

2.2.2 Microspheres

Microspheres were fabricated by melting the ends of optical fibers with a CO_2 laser beam. An $8 - 10$ cm length of bare optical fiber was stripped and cleaned as described above, using denatured alcohol to remove debris. The fiber was then clamped vertically to a linear translation stage (MT-XYZ from Newport). A small washer taped to the end of the fiber served as a weight for the tapering process (Fig. 2.3). The heating and melting process
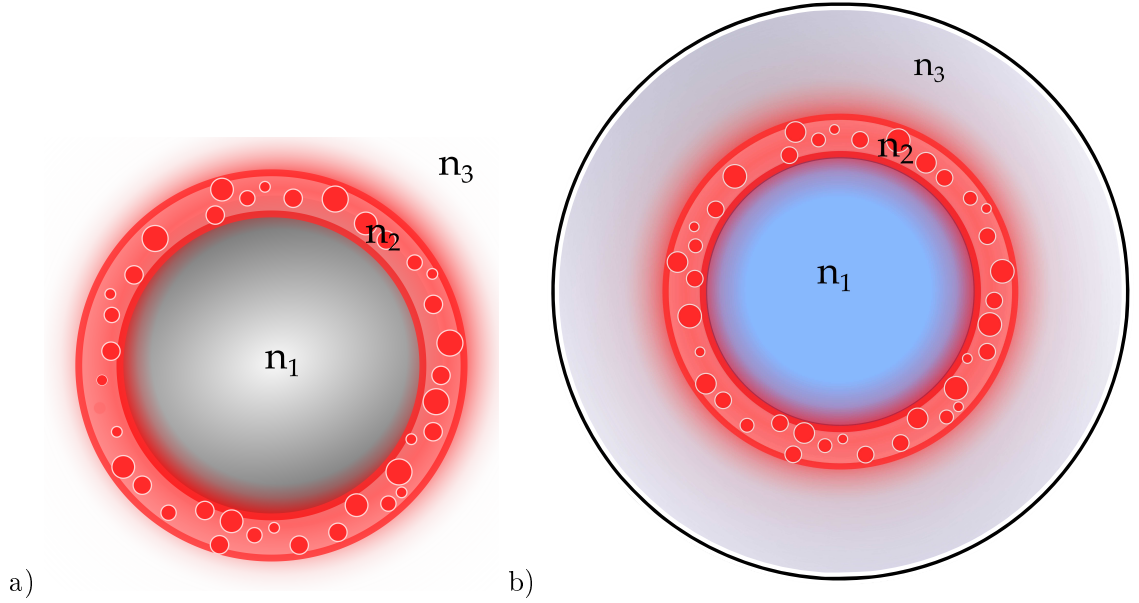
Figure 2.2: Cross-sectional profile schematic of a) a coated fiber and b) a coated microcapillary, illustrating the refractive indices n_1 (inner index), n_2 (QDs) and n_3 (outer index).

employed a ULR-10 CO_2 laser by Universal Laser Systems, operated at a wavelength of 10.6 μm, a rated power of 10 W, and a repetition rate of 5 kHz. The fiber was moved into the focus of the laser, while the laser duty cycle was set between 20-30% until the fiber started to stretch and taper. The fiber was pulled using the linear stage until a sufficient length of the fiber had been tapered (typically $\sim$ 5 cm). The length of the taper can determine the volume of the final microsphere. The fiber was then cut by increasing the laser duty cycle to around 60%. Next, the taper was melted in the focus of the laser until it formed a small melt-ball under surface tension. The rest of the taper was fed into the melt by moving the linear stage, until the taper was mostly consumed. Then the laser was turned off.

This finished bare microsphere was then removed and placed vertically in the custom quartz crucible. Before coating with HSQ, the microsphere was cleaned carefully with methanol to remove debris. Two coatings of HSQ were applied using the same process as described previously for the fiber. The stem and neck of the annealed microsphere was extremely brittle, so care was taken to store the microspheres such that the sphere did not snap off. Carbon-tipped tweezers were used to gently hold and transport the spheres by grasping the thick fiber stem.
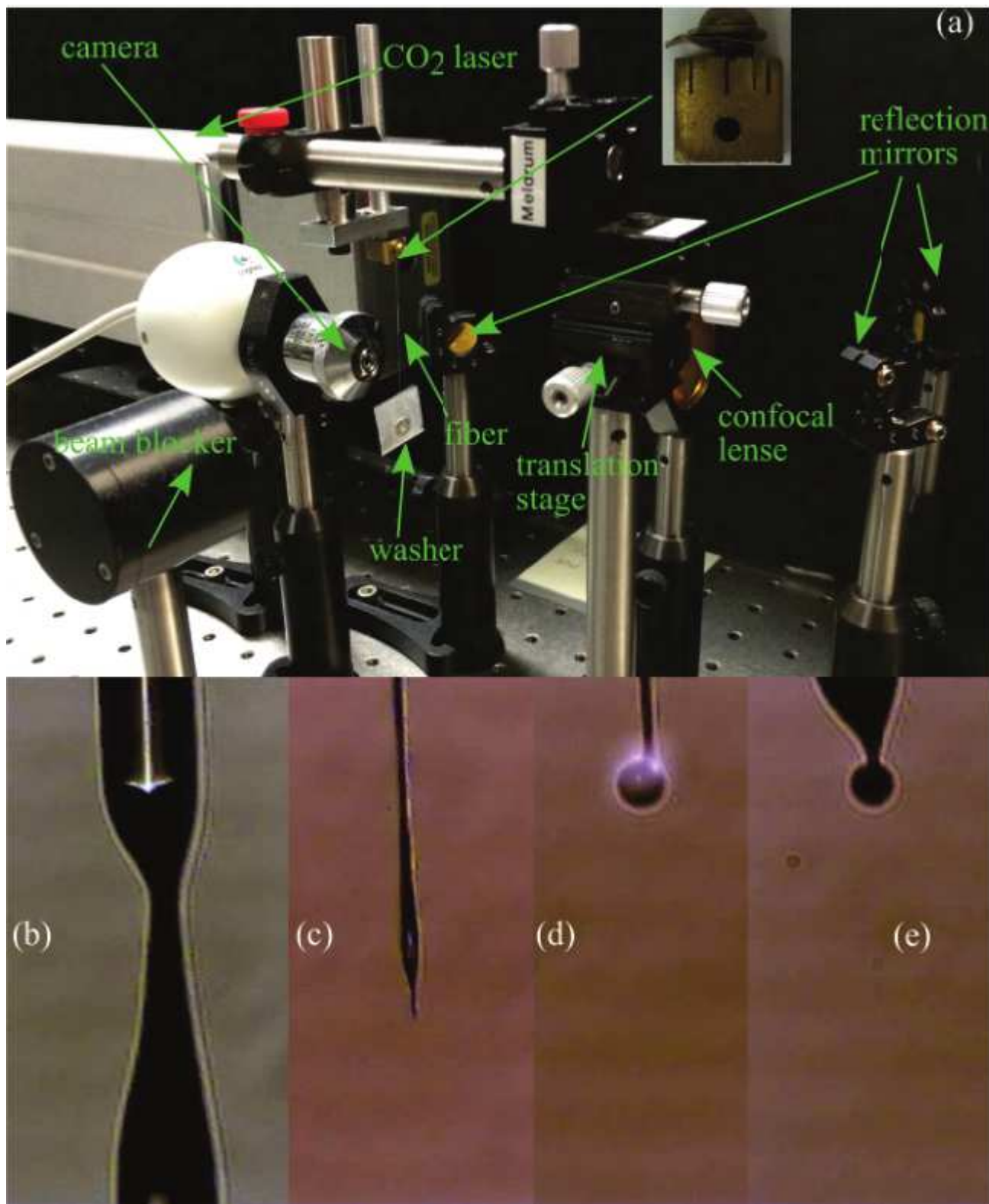
Figure 2.3: An overview of the microsphere fabrication process. a) The fabrication setup, with a fiber that will taper under the weight of a small washer. b) The fiber is at the focus of the CO_2 laser. The fiber starts to taper. c) The taper, after the weight has broken off. d) The taper melts in the laser beam and forms a sphere under surface tension. e) The finished microsphere. From Ref. [7]

2.2.3 Microcapillaries

Microcapillaries with a fluorescent coating in the inner channel (Fig. 2.2b) were prepared using slightly different methods as compared to those described above. A $5 - 10$ cm length of microcapillary (outer and inner diameters of 363 μm and 50 μm, Polymicro Technologies #1068150017) was cleaved from a spool and then heated in a furnace for 45 minutes at 650°C in an oxygen atmosphere. This removes (effectively ashes) the polyimide jacket. The resulting glass microcapillary was left to cool and then dipped into a vial of HSQ, so that the solution was drawn into the channel by capillary action. The resulting filled capillary was annealed in an atmosphere of 5% H_2 + 95% N_2 in two steps. The first step was for 1 hour at 300°C in order to evaporate the MIBK solvent, and the second step was for 1 hour at 1100°C in order to collapse the HSQ cage structure and precipitate the SiQDs [130]. The first step was deemed necessary for microcapillaries because the solvent is contained inside the capillary and does not evaporate as readily as it does from a fiber or microsphere surface.

2.3 Setup and mounting samples

2.3.1 Fibers

The experiments performed with QD-coated optical fibers required them to be immersed in various solutions while the QD fluorescence was measured. To mount the fiber into a fluidic setup, it was clamped onto an optical microscope with a machined clamp and held in place with a magnet. The clamp was then attached to a stage on the optical microscope, so that the fiber was mounted parallel to the spectrometer slit. A 700-μm-inner-diameter square capillary was then inserted into a 1.19-mm-inner-diameter polyethylene tubing and the joint was sealed with paraffin wax film. The square capillary was then clamped to a linear translation stage such that the fiber could be inserted into the channel. The square capillary thus formed an external fluidic chamber for the QD-coated fiber. The fiber was placed inside the capillary at a small angle so that one end rested on the inside wall, in order to establish mechanical support. The fiber setup and the microscope were protected from air currents in the room with an aluminum foil covering.

Lack of drainage was a problem in the setup. When the fluid reached the end of the

square capillary, it would form a droplet that gradually weighed down the capillary and fiber until the droplet fell. This caused unacceptable mechanical vibrations during data collection. One solution was to insert a wick attached to the "drainage end" of the capillary, as pictured in Fig. 2.5. This served to dampen the cantilevering effect and prevent fluid from dripping onto the objective lens. However, placement of this wick was finicky, and the wick was prone to movement over the course of the experiment.

Figure 2.4: Fluorescence image of the fiber showing the hypothetical spectrometer slit alignment.
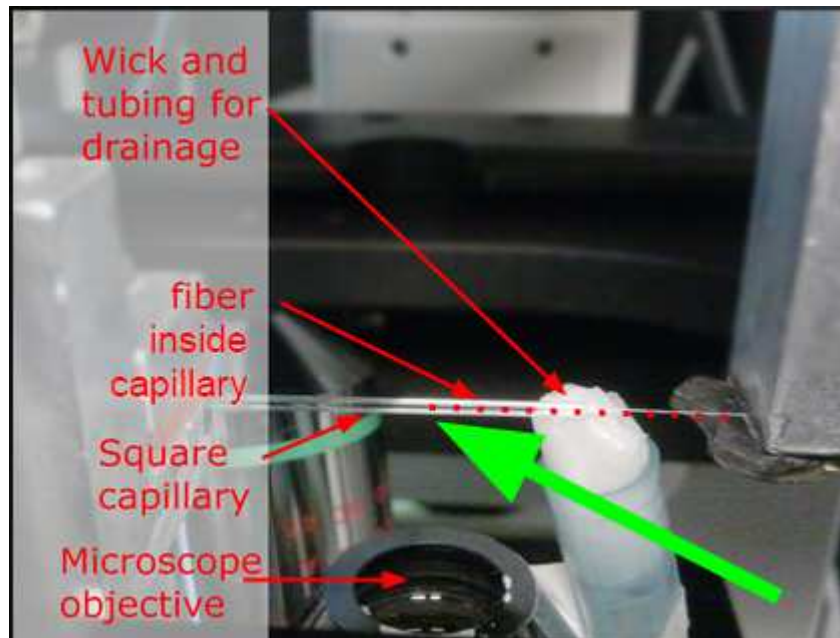
Figure 2.5: Image of the fiber sensor setup showing a fiber inserted inside a square capillary.

The fibers were oriented two ways: lengthwise or cross-wise with respect to the spectrograph entrance slit (Fig. 2.4). This changed the absolute direction of the TE or TM polarization. If the fiber was mounted parallel to the transmission axis of the analyzer, the electric field of the transmitted light was TE polarized with respect to the WGM propagation plane. In the opposite configuration (*i.e.* fiber axis perpendicular to the transmission

axis), the electric field was radial (corresponding to a transverse-H field, or TM polarized).

2.3.2   Microspheres

The microspheres were clamped with the same apparatus used for mounting fibers. The clamp was then attached to a stage on the microscope. The sphere was oriented so that the entrance slit of the spectrograph was parallel to the equator of the microsphere. The polarization state (TE or TM) was determined by the positioning of the transmission axis of the analyzer with respect to the sphere. The analyzer was rotated to change the measured WGM polarization state.

2.3.3   Microcapillaries

Microcapillaries were mounted onto a custom stage holder used for pumping fluids into the channel (Fig. 2.6). The capillary was first mounted on the holder with mounting wax. Next, 28 gauge (0.015 inch inner diameter) Teflon tubing was attached to the ends of the capillary with Norland Optical Adhesive #76. The same adhesive was used to attach the tubing onto the stage for support. The glue was cured with a broad spectrum UV lamp, and heated to 50℃ overnight. The other end of the tubing was attached to the top of the outer bars of the stage with craft glue (Fig 2.6). This provided two points of support that helped to minimize mechanical motion of the capillary. The holder was then mounted onto the microscope stage, with the capillary axis parallel to the spectrometer entrance slit, and left overnight to settle.

2.4   Fluorescent measurement and characterization

Once a SiQD-coated fiber, microsphere, or capillary had been successfully mounted in place on the microscope stage, the next step was to perform fluorescence spectroscopy. In order to excite the fluorescence, the samples were excited with one of:

(a) a 445 nm blue diode laser (Arctic from Wicked Lasers) with an incident power of $\sim 60\,\mathrm{mW}$ after optics,

(b) a 488 nm line of an Ar^+ laser with power of $\sim 15\,\mathrm{mW}$ after optics,
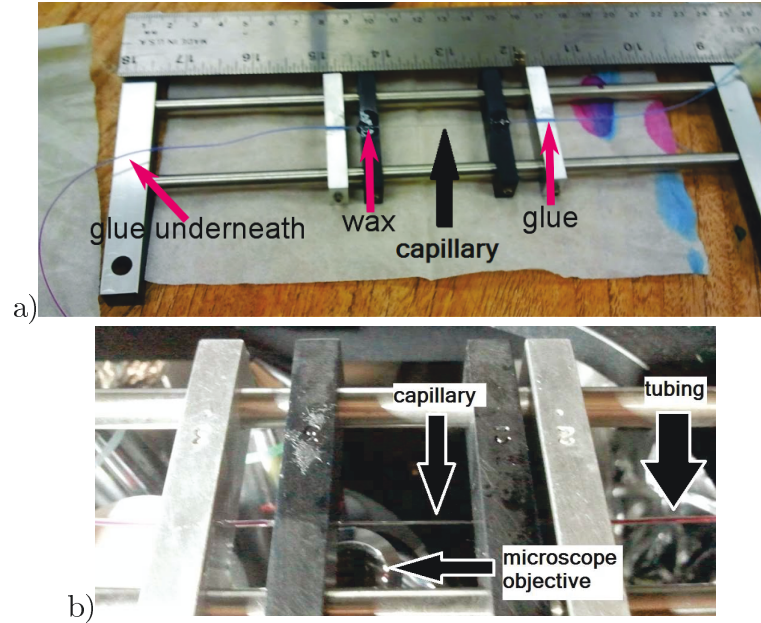
Figure 2.6: Image of stage holder used for the microcapillaries and associated tubing. Food colouring was inserted the tubing to make the progress of the solution visible in test runs. The images are a) the stage before mounting, and b) the stage mounted onto the microscope.

   (c) a 445-nmblue diode laser with a nominal output of $\sim 1W$ through the 20x microscope objective.

Both (a) and (b) were incident on the sample through free space, *i.e.* the beam was brought directly to the sample using external mirrors and lenses. In the case of (c), the beam was incident on the sample directly through the microscope objective.

   The fluorescence was collected by the microscope objective (usually 20x, NA=0.45), sent through a long pass filter to remove scattered laser light, and was then incident on the entrance slit of an LHIRES-III spectrograph (Shelyak Instruments) attached to the side port of a Nikon Eclipse TE 200-e inverted optical microscope. An analyzer was used to separate the TE and TM components of the fluorescence. The grating had a pitch of 76 pm ($\frac{d\lambda}{dpix} = \frac{58\,\mathrm{nm}}{765\,\mathrm{pixels}}$) and a manufacturer quoted resolution of $\mathrm{d}\lambda/\lambda = 17000$ around 656.281 nm. The spectra were imaged onto a Santa Barbara Instrument Group (SBIG) ST-7XME CCD camera cooled to $-15°$C. The spectral images were then retrieved with the manufacturer supplied software and saved as 16-bit gray-scale TIFF files. For "real time" measurements, the spectra were saved on a remote computer for live analysis.

To measure fluorescence lifetimes on flat films and microspheres, a different setup was used. The incident laser beam was modulated with an acousto-optic modulator (AOM) operating at 1 kHz, with pulse widths chosen from 10 to 500 μs. Fluorescence from the sample was collected with an optical fiber and fed into an OceanOptics USB2000 spectrometer to obtain a spectrum. The fiber was then attached to a water-cooled photomultiplier tube (PMT) and the fluorescence decay collected for 1 μs steps to obtain an average lifetime.

2.4.1 Calibration of wavelength and intensity

The spectra from all samples were wavelength-calibrated using the known spectral lines from a mercury-argon (HgAr) lamp. This provides a direct relation between the horizontal pixel number and wavelength. The wavelength calibration was automated with a script written in *Mathematica.*

The intensity calibrations were performed using a standard blackbody radiator with a colour temperature of 3100K (the LS1 tungsten-halogen lamp from OceanOptics). This correction has a simple mathematical form given by:

$$I(\lambda) = B(\lambda) \cdot \frac{I_s(\lambda) - I_b(\lambda)}{I_{bb}(\lambda) - I_b(\lambda)} \tag{2.1}$$

where $I(\lambda)$ is the corrected intensity, $B(\lambda)$ is the blackbody spectrum calculated from Planck's Law (T=3100K), and $I_s(\lambda)$, $I_{bb}(\lambda)$ and $I_b(\lambda)$ are the raw intensity, measured intensity spectrum of the blackbody radiator, and background (dark) intensity respectively. One can clearly see that $I(\lambda) = B(\lambda)$ when $I_x(\lambda) = I_{bb}(\lambda)$, as it should (*i.e.* the blackbody radiator will yield an exact blackbody intensity after correction). The accuracy of this correction depends on the LS1 light source yielding a true blackbody radiation spectrum.

2.5 Fluorescence lifetime imaging

Fluorescence lifetime imaging was performed on QD-coated microspheres in order to determine whether the Purcell effect might be observable. This process used an iStar DH734 intensified CCD (iCCD) from Andor Technology. The samples were pumped using either the Ar$^+$ laser or the blue diode laser, as described in Chapter 2.4. A function generator (Tektronix AFG3102 Dual Channel Arbitrary Function Generator) was used to control the

AOM and to trigger the iCCD. The fluorescence lifetime setup is fairly complex and was built in our lab first in this thesis; thus a detailed and complete description of the operation procedure is given below.

Several key factors are needed to describe the collection of a fluorescence lifetime "movie". Essentially the goal was to collect 1-μs image frames that could be sequenced into a movie. Each image must have a sufficient signal-to-noise ratio (SNR) so that the fluorescence lifetimes can be analyzed. To achieve this, one must control the exposure time, gate pulse width, and gate step (Fig. 2.7).

The exposure time controls how many gate pulses will be added to each frame. For example, during the first exposure time, the system adds all the gate pulses corresponding to the first microsecond time step (*i.e.*, photons arriving from 0-1 μs after the trigger. In the second exposure time, the system integrates pulses corresponding to the 1-2 μs gate pulses. This procedure continues until the desired number in the series (i.e., number of frames) is collected. Thus the total collection time is a product of the exposure time and the "number in series", with some additional read-out time added to the total. One problem to avoid is having the number of gate pulses overshoot the number of pulses that can fit in between triggers. If this situation happens, the pulse number takes precedence over the next trigger during collection and unexpected behaviour in the luminescence *vs.* time "movies" would occur.

The Andor Solis control software is used to set the acquisition parameters (Fig. 2.8). Several of the important configuration settings are shown in the screen capture. The exposure time, gate pulse width, gate step, and acquisition time are all controlled here. Additionally, one must select "kinetic series, and "external trigger" in order to perform lifetime imaging. "Integrate on chip" is necessary to increase the collection time by adding each gate pulse prior to the CCD readout (this works up to 2^{16} counts per pixel). The MCP gain controls the gain or amplification due to the Micro-Channel Plate in the iCCD.

2.6 Measuring WGM refractometric sensitivity

Part of the work in this thesis required a measurement of how much the fluorescence WGMs would shift in wavelength due to changes in the local index of refraction. This was achieved
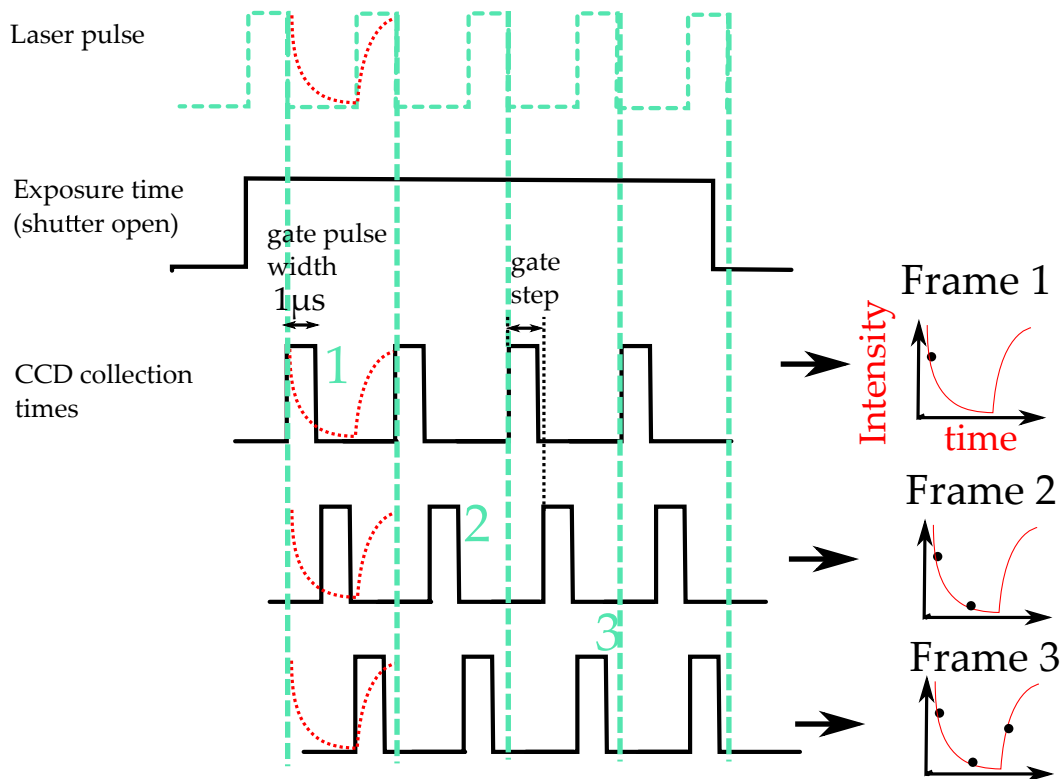
Figure 2.7: A schematic of the timing of the iCCD system. A digital delay generator controls the gate step (i.e. the time between the start of adjacent pulses). A schematic of the rise and decay of the fluorescence intensity in relation to the trigger is shown using red dots. The "number in series" must be less than the maximum number of frames that can "fit" between adjacent triggers. In the simplified diagram above, a maximum of three gate pulse widths can fit between the trigger signals.
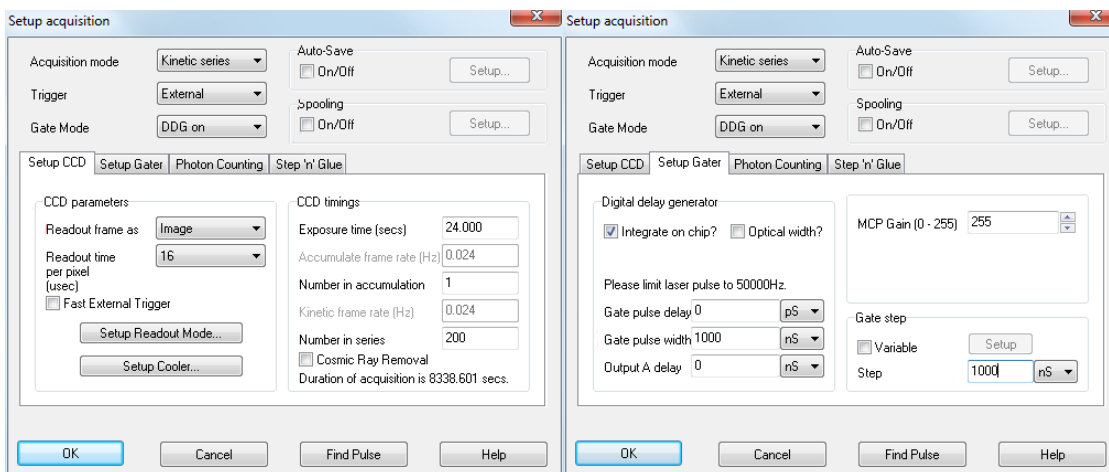
Figure 2.8: The image acquisition dialogue box in the Andor Solis control software. Shown are the settings to acquire a "kinetic series" (a "movie").

by pumping different solutions into a microcapillary or around an optical fiber that was coated with SiQDs. The solutions in this work consisted of sodium chloride in water (0.00 mol/L up to 2.50 mol/L) and ethanol-water solutions of varying concentration (Fig. 2.9). These solutions were easy to prepare and allowed a refractive index variation from 1.33 to 1.38 RIU.

In order to measure the sensitivity to local refractive index changes, the samples had to be exposed to at least two different solutions. Solutions were injected with 3 mL Beckton-Dickson plastic syringes and pumped through the capillaries with a Chemix Nanojet pump. However, simply switching the tubing to a different syringe on the same pump tended to cause thermal or mechanical fluctuations that affected the measurements. Therefore, a three-way valve was used to control the flow of different solutions into capillaries. However, the "dead volume" in the valve made it difficult to control the solution composition that reached the sensor. Therefore, an additional method was attempted in which different solutions were pre-pumped into a long tube, precluding the need for multiple syringes or valves.

The refractive indices of water and ethanol are well known. Dispersion formulae can be found in the literature for these substances at the near-infrared emission wavelength of the quantum dots. Pure ethanol has a dispersion formula of [136]

$$n = 1.35265 + 0.00306\lambda^{-2} + 0.00002\lambda^{-4}, \tag{2.2}$$

in nm. This gives a refractive index of 1.35748 at a wavelength of 800 nm.

However, the dispersion formulae for NaCl-water and ethanol-water compositions are not available at near-infrared wavelengths. Ref. [137] does give the refractive index formula for any NaCl-water composition at 589 nm and 700 nm wavelengths, but there are no dispersion formulas. Therefore, dispersion was ignored and data shown in Fig. 2.9 was used instead. This may lead to small errors in the sensitivity measurements, but they are expected to be minor because the effect of dispersion is small over the wavelength range investigated.

Temperature fluctuations can also affect the WGM resonance shifts via the thermo-optic or thermal expansion effects [100]. Therefore, the setup was enclosed within an aluminum foil and cardboard box to minimize the cooling effect of random air currents in the room. This also helped to minimize mechanical vibrations that could also occur due to air movement.
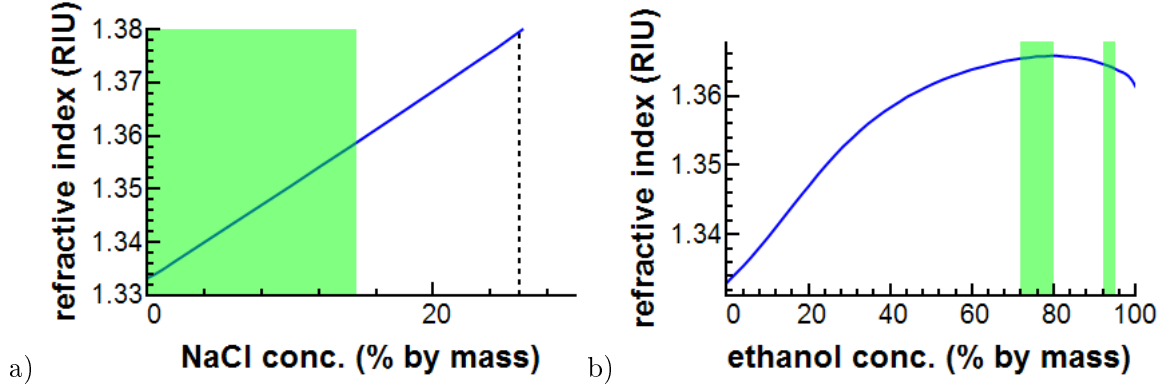
Figure 2.9: Plots of refractive index *vs.* concentration by mass in water at 589 nm wavelength and 20°C for a) sodium chloride-water solution, and b) ethanol-water solution. The vertical dashed line in a) corresponds to the saturation point for sodium chloride in water, ($\sim 26\%$). The green regions correspond to the concentrations or refractive indices used in this work. The ethanol-water plot was an interpolation from data taken from the CRC Handbook[9].

All measurements were taken at room temperature.

To determine refractometric sensitivity $\frac{\Delta\lambda}{\Delta n}$, one has to measure the change in the WGM wavelength due to known local refractive index change. Measurements over a range of RI were taken, a linear least squares fit performed, and the sensitivity extracted from the slope of the fit. Spectra were taken at regular intervals, for example 10 second exposures were continuously collected, as solution was pumped through the capillary or past the fiber.

2.6.1 Measuring WGM spectral shifts with Fourier analysis

The WGM shifts can be found with one of several methods. A common method is to find the peak by Lorentzian curve fitting. However, this method has several problems. First if the Q-factor is high, the mode may not be well sampled due to the pitch of the spectrograph (76 pm in our case). Second, overlapping radial order modes [129] can cause fitting algorithms to fail in some cases. Third, the WGMs in microcapillaries are asymmetric due to the presence of "spiraling modes" that overlap the main WGM [86]. For these reasons, curve fitting generally cannot capture mode shifts smaller than the pitch of the spectrograph system.

Here, we use the Fourier shift theorem to measure the WGM mode shifts. This theorem applies to a periodic waveform in which the only change is a phase shift. While a "pure shift" is not strictly the case in a WGM spectrum (*i.e.* different mode orders can have slightly different refractometric sensitivities), for small shifts the overall spectral waveform will re-

main approximately constant [129]. For a data set of N samples consisting of intensity $I(f_p)$ at frequency f_p, the discrete Fourier transform is [7, 129]:

$$I(f_p) = \frac{1}{N} \sum_{n=0}^{N-1} F_p \cdot e^{i2\pi \frac{p}{N-\Delta f} f_p} \tag{2.3}$$

where $p = 0, 1, ..., N-1$ is the number of samples (i.e. the number of pixels in the spectrum), and Δf is the sampling rate. For a uniform shift (i.e. a "pure shift"), the amplitude of the pth Fourier component F_p is given by

$$F_p = \sum_{n=0}^{N-1} I(f_p + f_s) \cdot e^{-i2\pi \frac{p}{N-\Delta f} f_p}, \tag{2.4}$$

where f_s represents the waveform shift in frequency units. The phase shift of the pth component can be written as

$$\Delta\phi = \frac{2\pi p f_s}{N \cdot \Delta f_s}, \tag{2.5}$$

so that the shift in frequency units is

$$f_s = \frac{N \cdot \Delta f_s}{2\pi} \left(\frac{\Delta\phi}{p} \right). \tag{2.6}$$

We want to obtain f_s from consecutive WGM spectra in order to quantify the spectral shifts.

In Eqs. 2.5 and 2.6, we see that $\frac{\Delta\phi}{p}$ is constant and depends directly on f_s. Therefore, a measurement of $\frac{\Delta\phi}{p}$ is needed to obtain the WGM spectra shifts. This is achieved by plotting $\Delta\phi$ vs.p for selected high-amplitude components of the WGM spectra and performing a weighted linear fit (with each ($\Delta\phi$, p) point weighted according to its power F_p^2 . This value was then inserted back into Eq. 2.6 in order to find the spectral shift f_s. The result can be converted into a wavelength shift via $\Delta\lambda = c\Delta f_s/f_c^2$ where f_c is the center frequency in the spectrum.

2.6.2   Sensorgrams for data analysis

Sensorgrams are a representation of the spectral shift over time. A change in solution RI can be monitored in sensorgram format by plotting the WGM wavelength shift as a function of time. All the data points in a sensorgram will have error bars associated with them. These

44

arise from the standard error for each point in the weighted linear fit discussed on the above page.

The refractometric sensitivity can be obtained from the sensorgrams as two different solutions are pumped through the capillary. The sensitivity is given by $\Delta\lambda/\Delta RIU$, where $\Delta\lambda$ is obtained from the mean shifts obtained for each solution in the capillary. In some cases there was an underlying drift in the sensorgram data. This was handled by linear least squares fitting of the sensorgram data prior to any refractive index changes, and then subtracting the fit (*i.e.* the drift) from the data.

Chapter 3

The search for Purcell enhancement

3.1 Characterization of silicon quantum dot film

In order to search for evidence of the Purcell effect in an ensemble of quantum dots on a microsphere, the quantum dot lifetime needs to be measured. First a flat film consisting of silicon QDs embedded in an oxide matrix was prepared on a quartz wafer for comparison to the QD-coated microsphere. This sample was prepared by spin coating and annealing a layer of HSQ on a fused silica substrate, using the methods described in Chapter 2.1. The luminescence peaked at around 810 nm (Fig. 3.1c). The fluorescence decay was measured in order to provide a comparison to the QD luminescence dynamics on a microsphere (Fig. 3.1a).

3.1.1 Nonlinear model fitting

Ensembles of quantum dots can be modeled with a mathematical function called a stretched exponential, also known as a "Kohlrauch" function [138, 139, 140, 141, 142] :

$$A \exp(-(\frac{t}{\tau})^{\beta}) + C \qquad 0 \leq \beta \leq 1. \tag{3.1}$$

Here, τ is a lifetime parameter, β is a stretching parameter, A is the amplitude and C is the offset.

The stretched exponential function empirically describes a relaxation process that has a distribution of rates, such as the discharge of a capacitor [143] or even a socio-economic model of success [144]. It is widely used to model luminescence decays [141, 145, 146, 147] when the decay cannot be adequately modeled by a single exponential. The stretched
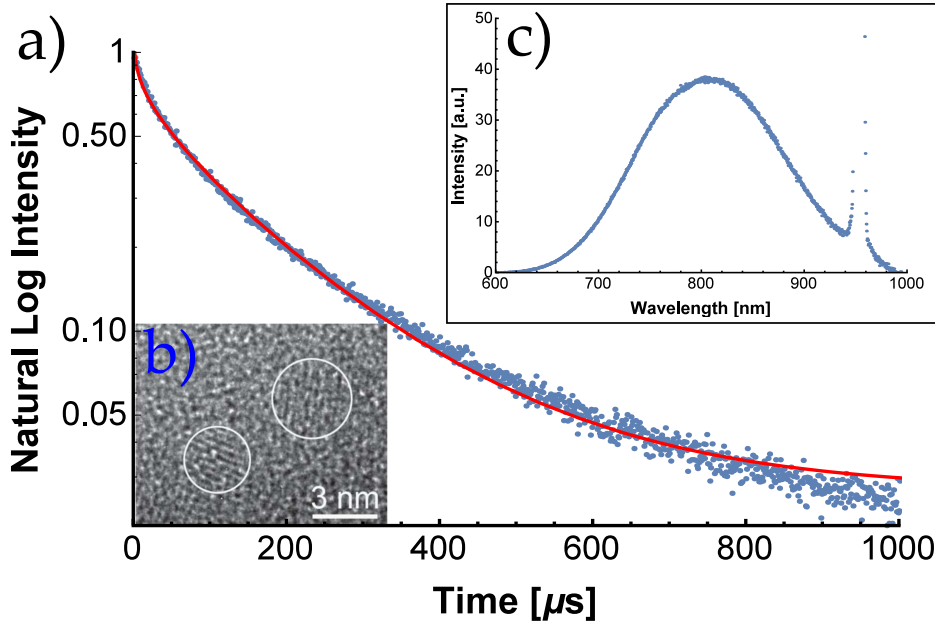
Figure 3.1: a) The fluorescence decay for a thin film of HSQ on a quartz wafer annealed at 1100°C, excited with a 445 nm blue diode laser. Also shown is a fit with a stretched exponential function (Eq. 3.1.4, see text), where $A = 108.95$, $\beta = 0.89360$, $\tau = 158.24$ μs, and $C = 0.026993$ (4.1.1). b) A high-resolution TEM micrograph from a flat Si-QD film showing silicon quantum dots (circled regions), from Ref. [8] c) The fluorescence spectrum for a thin film of HSQ on a quartz wafer annealed at 1100°C excited with a 475 nm Ar$^+$ laser. The sharp peak at $\lambda = 950$ nm is a higher order grating interference maxima due to the pump laser.

exponential function can be used to gauge differences from the single exponential decay using the stretching parameter β, providing a means of comparison to other results in the absence of a more fundamental model [138].

The stretched exponential is a widely used model for the fluorescence decays of quantum dot ensembles [140, 142, 145, 146, 147, 148, 149]. However, the origin of the behaviour that gives rise to the stretched exponential in ensembles of quantum dots is heavily debated and there exists a range of explanations [141, 146]. When the behaviour is related to the size distribution in QD ensembles, the model assumes a distribution of QD lifetimes *a priori*, where for the stretched exponential the lifetime distribution is the inverse Laplace transform of the fluorescence decay [138]. Recovering the distribution can be mathematically complicated and generally requires numerical modeling [141, 142, 149].

The key parameters of the model are the "lifetime" τ and the stretching parameter β. The physical meaning of τ, in terms of a fluorescence decay, is related to the average lifetime of the ensemble by

$$\langle\tau\rangle = \tau\beta^{-1}\Gamma\left(\frac{1}{\beta}\right) \tag{3.2}$$

where $\Gamma(\frac{1}{\beta})$ is the mathematical Gamma function [138, 141]. Single quantum dots have single exponential decays ($\sim \exp(-\frac{t}{\tau})$), but an ensemble has a distribution of lifetimes related to the QD size distribution [146]. The parameter β, which is between 0 and 1, can be used to recover the ensemble lifetime distribution through an inverse Laplace transform [138]. A small β indicates a broad lifetime distribution and a β value approaching 1 conversely indicates a narrow distribution [141]. When $\beta = 1$, the single exponential decay is recovered.

One consideration is that the stretched exponential, as given in the form of Eq. 3.1, describes the population decay, but what is actually measured is the luminescence decay. Eq. 3.1 is used by many references to model the luminescence decay directly, but this is not technically the appropriate form of the stretched exponential function. The luminescence decay $I(t)$ is generally related to the fractional population of excited emitters at a certain time t', such that the intensity in a given time interval is given by

$$\int_{t=0}^{t=t'} I(t)\,dt = 1 - \frac{n(t')}{n(0)} \tag{3.3}$$

where $\frac{n(t')}{n(0)}$ is the fraction of the initial population that remains excited. For stretched exponential population decays, Eq. 3.1 is equal to $\frac{n(t')}{n(0)}$. The luminescence decay would then be the derivative of the right hand side of Eq. 3.3 [141]:

$$I(t) = A\frac{\beta}{t}(\frac{t}{\tau})^\beta \exp(-\frac{t}{\tau})^\beta + C \tag{3.4}$$

where the fitting parameters are A, τ, β, and C are as defined before.

For an ensemble of QDs on a cavity, one expects τ and β to be different for QDs on resonance $vs.$ off resonance. Due to the Purcell effect, QDs on resonance would have a smaller (faster) lifetime, and QDs off resonance would have a larger (slower) lifetime. This would manifest as a change in the lifetime distribution. In previous work, for example, it was shown that such a situation would show a decrease in β and an increase in τ, compared

to the situation where the ensemble was *not* coupled to a cavity [113]. This represents the overall effect of a distribution of emitters that are continuously "spread" over many cavity modes.

3.1.2   Quantum efficiency

The quantum efficiency (QE) of a quantum dot is the ratio of photons absorbed to the number of photons emitted and can be written as:

$$\eta_R = \frac{number\ of\ photons\ emitted}{number\ of\ photons\ absorbed} = \frac{1}{1 + \tau_R/\tau_{NR}} \tag{3.5}$$

Quantum dots with high QE (ie. large η_R) have short radiative lifetimes (τ_R) compared to non-radiative lifetimes (τ_{NR}) (ie. $\tau_R \ll \tau_{NR}$). In a decay measurement such as that shown in Fig. 3.1, the observed decay rate is the sum of the radiative and non-radiative ones, *i.e.*

$$\frac{1}{\tau} = \frac{1}{\tau_R} + \frac{1}{\tau_{NR}}, \tag{3.6}$$

Therefore the observed decay rate is related to the QE. Although we could not measure the QE directly since there was no locally available apparatus to do so, the quantum efficiency of silicon quandum dots can be as high as 68% for functionalized QDs in solution [150]. The values in oxide films are likely to be less, *i.e.* on the order of a few percent [151, 152].

3.2   Characterization of microsphere fluorescence

The whispering gallery modes were clearly evident in the PL spectrum from the QD-coated microsphere (Fig. 3.2a). The visibility was 0.1, the Q-factors were ∼800, and the FSR was ∼ 7.2 nm, consistent with a 25-μm-diameter microsphere. The PL image shows that the characteristic red emission is concentrated around the equator of the microsphere and the fiber to which it is attached (Fig. 3.2c). The mode visibility was fairly low, indicating a significant fraction of uncoupled PL. The ensemble PL decay was fit with the stretched exponential function (Eq. 3.4) as discussed in the previous section, yielding $\tau = 156.8\ \mu$s and $\beta = 0.89$ (Fig. 3.2b).
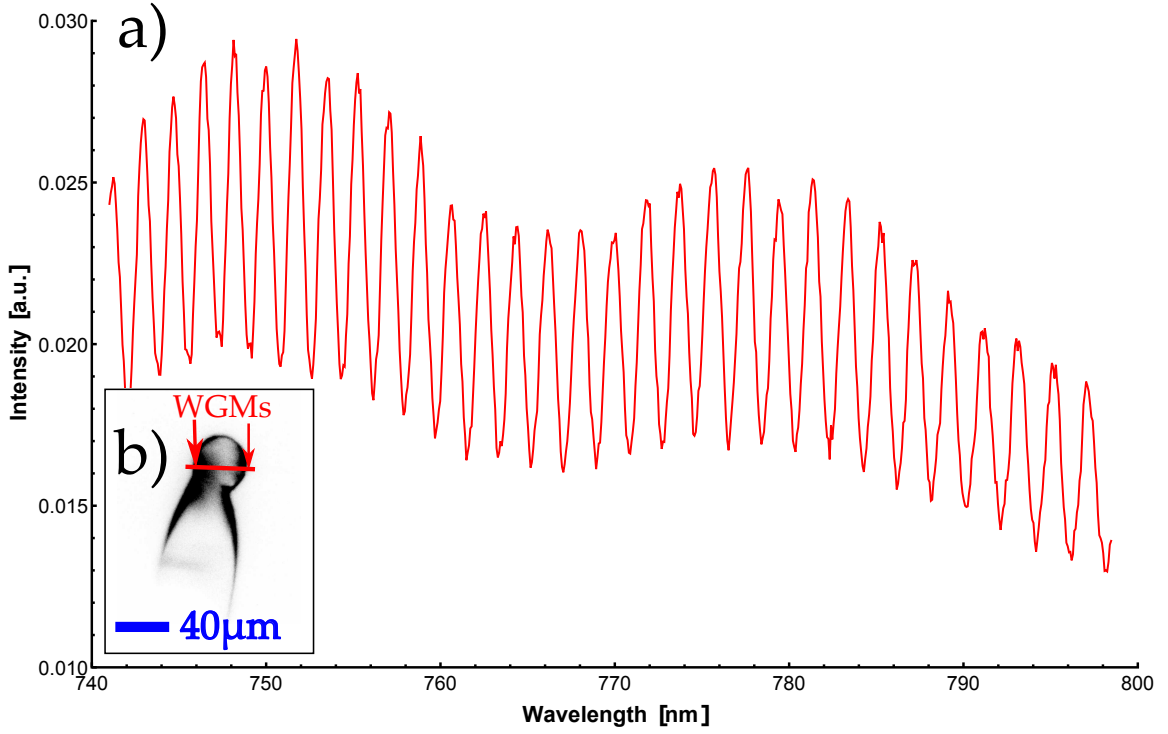
Figure 3.2: a) The WGM spectrum for SiQDs on a microsphere. b) Fluorescence image of a microsphere coated with SiQDs. The slit position corresponds to the red line and the WGMs are strongest at the positions indicated.

3.3 Microsphere lifetime imaging

In order to search for evidence of the Purcell effect, a fluorescence decay "movie" was obtained using the fluorescence lifetime imaging method described in Chapter 2.5. Frames corresponding to several different time intervals are illustrated in Fig. 3.3. The overall decay, as taken from one specific pixel on the edge of the sphere, clearly indicated the non-exponential nature of the luminescence decay (Fig. 3.3), which would otherwise appear as a straight line on the semi-log plot.

In order to construct lifetime "maps", the microsphere area was first converted into polar coordinates. Next the data for each pixel were normalized to the peak value. Once this was done, each decay was fit using the stretched exponential function given in Eq. 3.4. Because the results consisted of numerous fairly noisy luminescence decays (*i.e.* one for every image pixel), the fits required good initial guesses in order to successfully converge. This process was partly automated by taking the time at which the intensity had reached $1/e \approx 0.37$ of

its initial value as the starting guess on each pixel. The starting guess for β was simply fixed at 0.6. For example, for the pixel indicated by the red star in Fig. 3.3, the fit parameters are $A = 11.5$, $\tau = 22.5\ \mu\text{s}$, $\beta = 0.976$, and $C = 0.00632$. Also shown are the 90% confidence bands of the fit. The sharp drop at the beginning of the fit is an artefact from the fact that for time $t = 0$, Eq. 3.4 becomes infinite. The fitting process was then repeated for pixels all over the sphere (Fig. 3.4). The fitting parameters τ and β were then plotted with respect to the polar coordinates on the image in order to detect any trends.
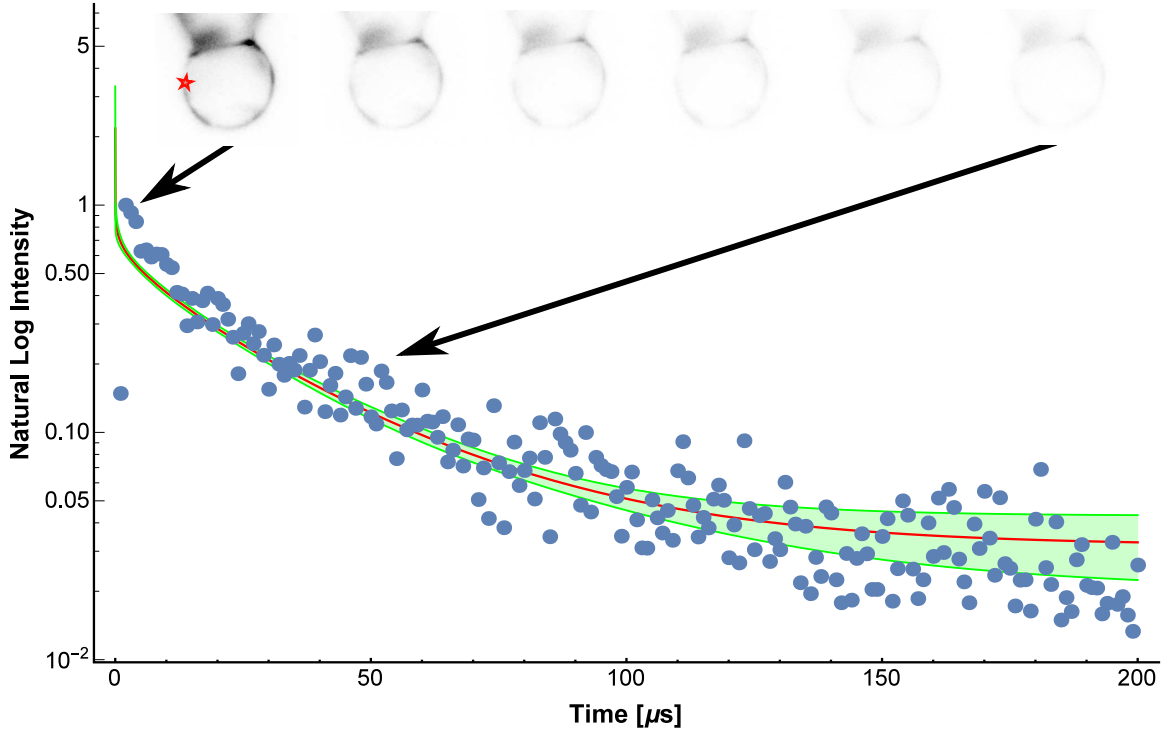
Figure 3.3: The luminescence decay for a specific pixel on the microsphere, as indicated by the red star in the image frames shown across the top. The fit and confidence bands are discussed in the text.

For a cavity-coupled QD ensemble, the stretched exponential parameters τ and β were predicted to increase and decrease, respectively as a result of part of the ensemble being on-resonance and part being off-resonance [113]. However, no clear trends were observed either in the angular or radial directions (Figs. 3.4). The values for τ were typically on the order of 30 μs and β was around 0.83, although the data is also fairly noisy. Since the WGMs are most pronounced along the equator (where the neck defines a "pole", one might expect the strongest effects to be seen there. The lack of any clear trends indicates no discernible
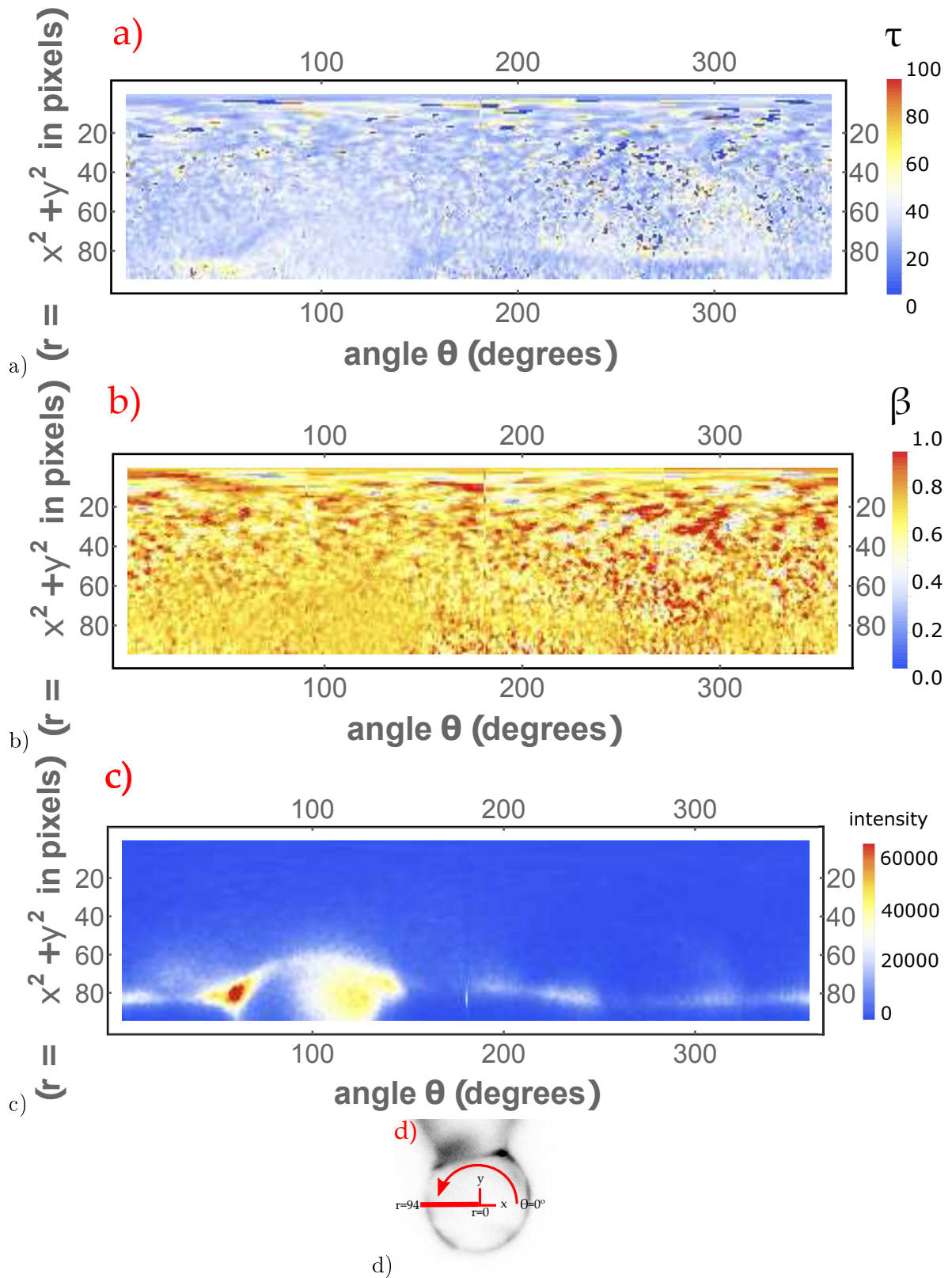
Figure 3.4: Colour map of the fitting parameters: a) τ; b) β; and c) the intensity over the entire sphere. The plots are in radial coordinates, from the center to edge along the line indicated on the sphere in d). The center of the microsphere is at the top of the images, and the "edge" of the microsphere is between r=78 to 86. The high intensity area is at the neck of the sphere.

52

Purcell effects. In other words, regardless of whether we look where the WGMs are strong or where they are weak, we observe no clear differences in the luminescence decay.

Therefore one can conclude that there is little evidence of Purcell enhancement or suppression in the current data. There are several possible explanations for this negative result. First, and perhaps most likely, the QE may be too low to observe clear Purcell effects. A low QE means that non-radiative processes dominate the decay (*i.e.* if $\tau_{NR} \ll \tau_R$). The Purcell effect only modifies the radiative rate, so if the QE is low, the overall rate will change comparatively little. Second, the cold-cavity Q-factor of the microsphere may be somewhat low (measured to be $\sim 10^5$ [7]) to observe significant rate modifications. Third, the linewidth of the QDs may be too broad (see chapter 1.5.2). Finally, not all the fluorescence may come from QDs that are well-coupled to WGMs. In future work, spectrally separating the fluorescence into resonant and non-resonant wavelengths, which was not possible at the current time, and measuring the decays seperately may be beneficial in determining the effects on the decay.

Chapter 4

Cavity-coupled Si-QDs for refractometric sensing

In the previous section, the resonant wavelengths of each WGM depended on the refractive index of the surrounding medium. Therefore, the next project was to determine the ultimate refractive index sensor performance, in terms of the overall detection limit. Fluorescent sensors have many advantages: the absence of complex and expensive equipment, the relative ease of use compared to other sensors, and their low cost of fabrication. However, their limit of detection (LoD, or detection limit) tends to be fairly modest (Table 4.1).

The nominal detection limits of fluorescent sensors are rarely demonstrated experimentally. For example, the best LoD calculated for a fluorescent microcavity is 10^{-5} RIU, while the best experimental observations are typically is in the range of 10^{-3} RIU to 10^{-2} RIU (Table 4.1). The objective of this chapter is to experimentally measure the ultimate detection limit, using an SiQD coated optical fiber or capillary as the sensor.

The most important advantage to employing a fluorescent optical fiber rather than a microsphere is that the mode structure should be identical along the length of the fiber. Thus, one can perform vertical binning on the WGM spectrum by aligning the fiber axis parallel to the spectrometer entrance slit and projecting the spectrum onto a 2D CCD. This should enhance the SNR and improve sensor performance [129]. Other advantages include the ease of fabrication and handling.

Smallest ΔRIU measured	Quoted LoD	Device	Ref.
3×10^{-2}	–	lasing dye in capillary	[153]
6.53×10^{-2}	5×10^{-4}	dye doped microspheres	[154]
2×10^{-2}	2.4×10^{-4}	lasing dye doped microspheres	[155]
7.55×10^{-2}	4×10^{-4}	QD embedded microspheres	[156]
5.52×10^{-2}	7.2×10^{-3}	QD coated optical fiber	[89]
10^{-3}	3×10^{-4}	dye doped microspheres	[157]
–	2.5×10^{-5}	QD coated bottle resonator	[99]
1.20×10^{-3}	–	QD coated microcapillary	[129]
2.10×10^{-3}	2.2×10^{-4}	QD coated microsphere	[83]
9.8×10^{-3}	1×10^{-3}	fluorescent polymer coated microcapillary	[128]
–	3×10^{-4}	dye doped microsphere	[158]
–	1.35×10^{-4}	QD coated microcapillary	[159]
–	8×10^{-5}	lasing dye doped microsphere	[123]

Table 4.1: A sample of the quoted LoDs and smallest measured refractive index changes for fluorescent WGM-based sensors in the literature.

4.1 Detection limits: modeling

In order to gain insight on the effect of using a two-dimensional CCD array to measure the WGM wavelength shift, we first conducted a set of basic data simulations. The aim was to investigate possible beneficial effects of projecting the WGM spectrum onto a 2D CCD array rather than onto a linear array. The simulated 2D WGM spectrum shown in Fig. 4.1 corresponds to a set of Lorentzian peaks plotted in greyscale along the horizontal (*i.e.* wavelength) axis, with Gaussian noise added. The vertical axis simply represents repeats of the same spectrum with random noise. This corresponds to the situation in which the spectrometer entrance slit is aligned perfectly parallel to the edge of an optical fiber or capillary, causing light from the WGM region to be imaged along the entire slit length. A "normal" 1D spectrum would thus simply be the intensity plotted along a single horizontal line of pixels in Fig. 4.1.
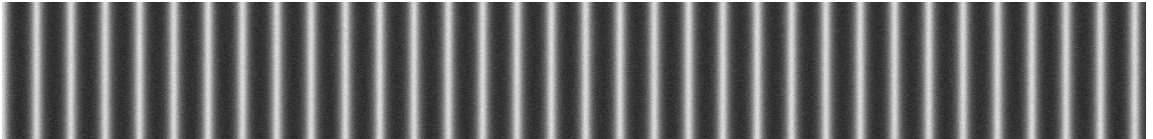
Figure 4.1: Simulated 2D WGM spectrum. The horizontal axis is wavelength.

The simulation shown in Fig. 4.1 represents a spectrum that is 1667 pixels wide, 200

pixels high, and contains Gaussian noise that gives a linear SNR of 100 (where SNR is calculated with respect to the mean signal amplitude over the whole spectrum). Therefore, one might hope that a simple vertical binning would improve the SNR by the square root of the number of vertical pixels, and thereby potentially also improve the ability to detect slight changes in the mode central positions, which is what one wants to measure for refractive index sensing.

The next step was to generate a set of 30 spectral images that incorporated a small spectral shift (0.167 pixels in this case). We don't show all the images here as it would be repetitive and such a small spectral shift is impossible to observe by eye. The spectral shifts were analyzed using the Fourier shift theorem, as described extensively in Refs. [7, 129, 160] and outlined briefly in Chapter 2.6.1. The strongest five Fourier components were chosen to contribute to the analysis. Fig. 4.2a shows the single-line result; in other words, the sensorgram that would be measured on a linear 1D CCD. While the shift is certainly detectable, the data are scattered and the errors from the fitting analysis are large. In comparison, Fig. 4.2b shows the same shift as it appears on a 2D CCD with vertical binning. The improvement is striking. Even larger improvements might be expected in practice, as typical scientific imaging CCDs have more than 200 vertical pixels. The one used in the data shown later in this chapter has 510 pixels in the vertical dimension.

However, there is a complication: quite often in experiment the WGMs do not form perfect vertical lines in the spectral image, but instead show some "waviness". This can be due, for example, to variations in the QD film thickness along the length [159] of the fiber imaged onto the slit, which translates the WGM mode positions. If this effect is not avoidable experimentally, it needs to be taken into account because it would otherwise blur the modes after the vertical binning step. In order to deal with this potential problem, an option was therefore installed in which the code would first calculate the mode shifts for all of the individual lines and take the sensorgram from the *average* of all the shifts. This in fact produced results identical to those shown in Fig. 4.2b, except that the error bars associated with the Fourier shift theorem for each shift cannot be similarly averaged in a meaningful way. Regardless, this method can account for "wavy" WGM spectra along the length of a sample, assuming that the magnitude of the shifts is always effectively the same.
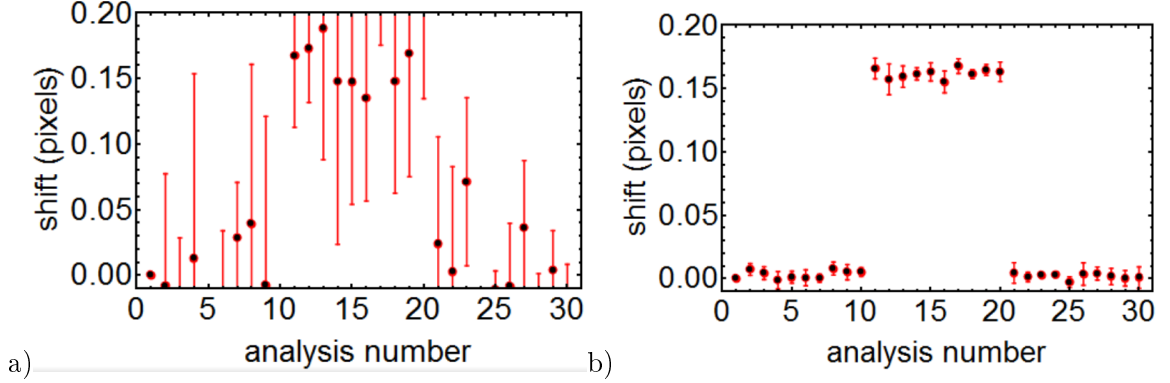
Figure 4.2: a) Sensorgram of a single line of the simulated 2D WGM spectrum. b) Sensorgram of the vertically binned spectrum. The shift of the middle ten spectra is +0.167 pixels in both cases.

This only drawback is that the method is more computationally intensive because it requires numerous Fourier transform steps.

Finally, the minimum 3σ shift, in pixels, can be found for any particular signal-to-noise ratio. For the case of a linear SNR of 100, corresponding to the data in Figs. 4.1 and 4.2, the minimum detectable pixel shift can be estimated by finding the standard deviation of the points for a constant (*i.e.* zero) shift and multiplying by three, resulting in a shift detection limit of 0.009 pixels in this case. This would be the ultimate limit achievable for a CCD of this size with an SNR of 100. This corresponds to the somewhat amazing wavelength shift of 0.7 pm for our detector, which has a pitch of 76 pm/pixel. Of course, one can expect that a number of experimental problems will cause the detection limit to be significantly larger in practice. This is what we next set out to determine experimentally, using the 2D spectral imaging method described above.

4.2 Experimental sensitivity and LoD of the fluorescent fiber sensor

The wavelength shift resolution was discussed and simulated in the previous section; here, it is necessary to determine the refractometric sensitivity of the device structure. In order to determine the sensitivity, a QD coated optical fiber was mounted onto the microscope stage in the fluidic setup described in Chapter 2.6. Theory suggests that the TM-polarized WGMs should be slightly more sensitive than the TE ones [86], so the analyzer was oriented with

its transmission axis in the radial direction (*i.e.*, perpendicular to the fiber axis). The slit was aligned parallel to the edge of the fiber in order to collect the 2D spectral images. The modes were relatively straight (vertical) in the spectral image, although there were some significant intensity variations (Fig. 4.3a), which corresponded to visibly brighter regions on the fiber. The 1D fluorescence spectrum (Fig. 4.3) showed a clear set of WGM oscillations, with a visibility of 0.02, a Q-factor of ~ 900, and a free spectral range of ~ 1 nm.
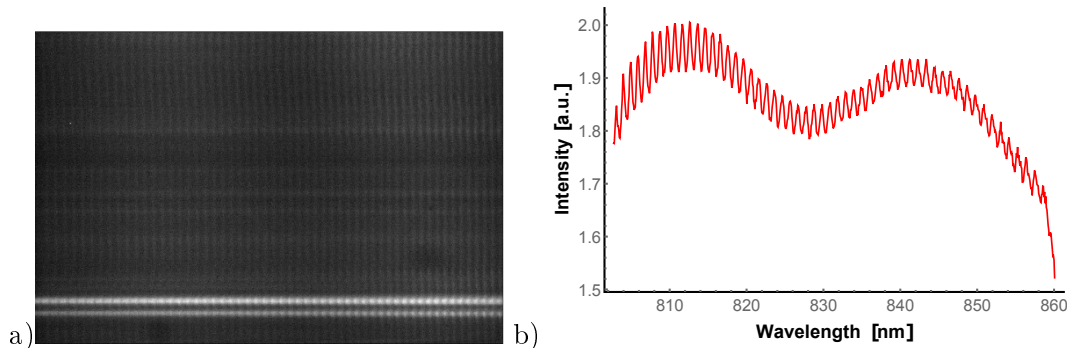
Figure 4.3: (a) Spectral image (TM polarization) taken along the length of the optical fiber. The vertical direction corresponds to length along the fiber, the horizontal axis is wavelength, and the greyscale is the fluorescence intensity. (b) The corresponding 1D spectrum made by vertically binning the intensity data in (a).

The overall limit of detection depends on two key parameters: the sensitivity S and the wavelength shift resolution R, such that LoD = R/S. A small LoD is desirable. The limit of detection obtained for a typical 1D spectrum ($\sim 10^{-3}$ RIU) is respectable for fluorescence sensors but is not particularly outstanding (Table 4.1). The measured sensorgram (Fig.4.4) suggests that one of the more significant problems was the noise in the experimental data. Thus we looked for experimental means to improve the overall result. First, any mechanical motion arising from air currents in the room was reduced by wrapping the setup in a foil enclosure. Second, a small wick was applied to the open end of the square capillary in order to minimize the unwanted cantilever motion that would typically occur whenever a fluid drip was released into the disposal container. Third, a system was developed in which the tubing would be pre-filled with sequences of solutions so as to minimize the motions associated with switching the valves when changing fluids. Finally, although this was mainly for convenience, a remote data collection system was developed which permitted the sensorgram to be continuously updated during data collection. This made it easier to

see what was happening in "live time".

Next, fluids having two different indices of refraction were pumped sequentially into the square capillary, which acted as the "chamber" for the fiber, as described in Chapter 2.6. The pumping sequence was in order, $2.405 \text{ M} \rightarrow 2.027 \text{ M} \rightarrow 2.405 \text{ M}$ NaCl solution. The corresponding refractive index change was 0.0039 RIU. This sensorgram (Fig. 4.2.2) was obtained only from the brightest row of the 2D spectrum (Fig. 4.3) using the methods described in Chapter 2. The two strongest Fourier components of the WGM spectrum were taken for the sensorgram analysis. The resulting sensorgram showed that the two solutions could be well detected, although there was a significant underlying scatter in the data. The sensitivity of this fiber was estimated from this data to be 20.7 nm/RIU. The experimental shift resolution in Fig. 4.2.2a was found to be 50 pm. This gives a LoD of 2.4×10^{-3} RIU (using $\text{LoD} = R/S$) with 99.7% confidence.
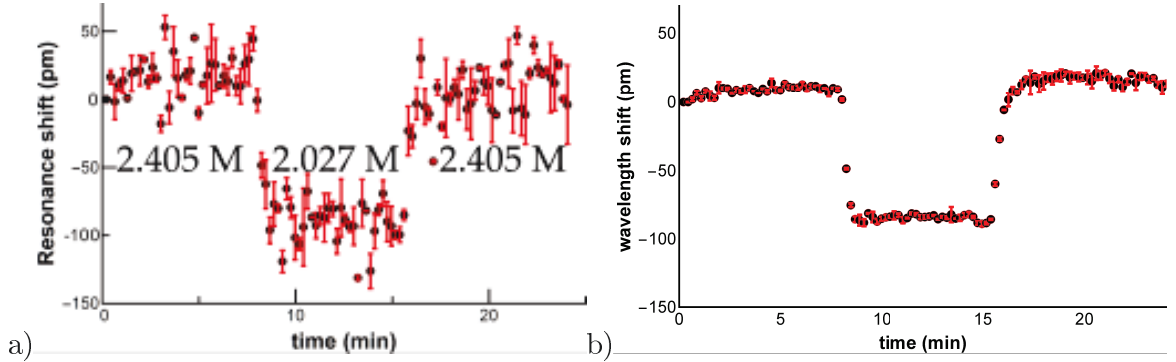
Figure 4.4: (a) Sensorgram corresponding to $\Delta \text{RIU} = 3.9 \times 10^{-3}$ RIU, measured from 1D line spectra. The error bars are due to the weight fitting in the Fourier shift method, as usual. (b) A sensorgram taken from the same data, but this time with full vertical binning.

The next step was to try the 2D WGM shift processing method discussed previously using experimental spectra in order to see if any improvement could be achieved. The 2D spectrum was vertically binned and the shifts measured from the binned data. A clear improvement in the SNR is observable by using the vertical binning method (Fig. 4.4b). The 3σ deviation decreased from 50 pm to 6 pm on going from the single line to the vertically binned analysis, respectively. The resulting LoD should therefore increase by a factor of ~ 8.

We finally compared the theoretical LoD with the best experimental one. From the previous analyses, for a sensitivity of 20.7 nm/RIU and an idealized minimum 3σ shift resolution

of 6 pm, the LoD should be 2.9×10^{-4} RIU. Therefore, another experiment was performed in which the NaCl concentration was changed from 2.216 M to 2.121 M, corresponding to ΔRIU $= 9.7 \times 10^{-4}$ RIU, which is only about 3 times larger than the theoretical one. This change was clearly detectable (Fig. 4.5) and smaller than any of those reported in Table 4.1. The largest issues appear to be systematic underlying drifts that could be due to mechanical motion that always seemed to plague the experiments, or possibly due to heating caused by the pump laser. Additionally, the film was not very constant along the length of the fiber, *i.e.* there were significant variations in the overall brightness in different regions. This implies that the vertical binning method might not improve the results as much as expected. For example, in the extreme case all the intensity would be in a single line and the binning would only contribute noise.
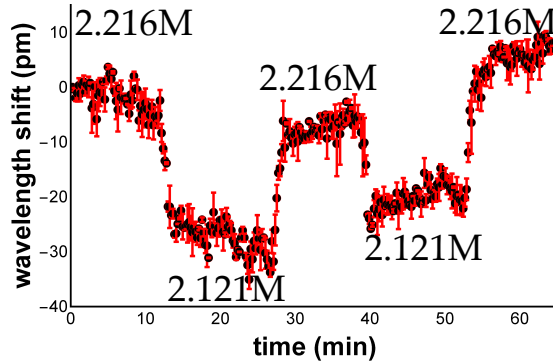
Figure 4.5: Sensorgram for a sequence of fluids for which the NaCl concentrations are labeled above the corresponding data. The shift was ΔRIU$=9.7 \times 10^{-4}$ RIU.

4.3 Sensing with a fluorescent microcapillary

From the experiments in the previous section, the fiber sensor was considered too fragile to produce a sufficiently stable sensing response. Mechanical motion and drift seemed almost unavoidable, probably because the fiber was simply inserted into one end of the square capillary "chamber" and was not supported inside the capillary. Thus, motion of the fluids could cause cantilevering or other types of unwanted motion. At this point, it was thought that a fluorescent-core microcapillary (as described in Chapter 2) with a layer of quantum dots on the channel surface would be a more stable system to investigate. As in the case of a fiber, a capillary can be imaged with the entrance slit parallel to the channel, allowing
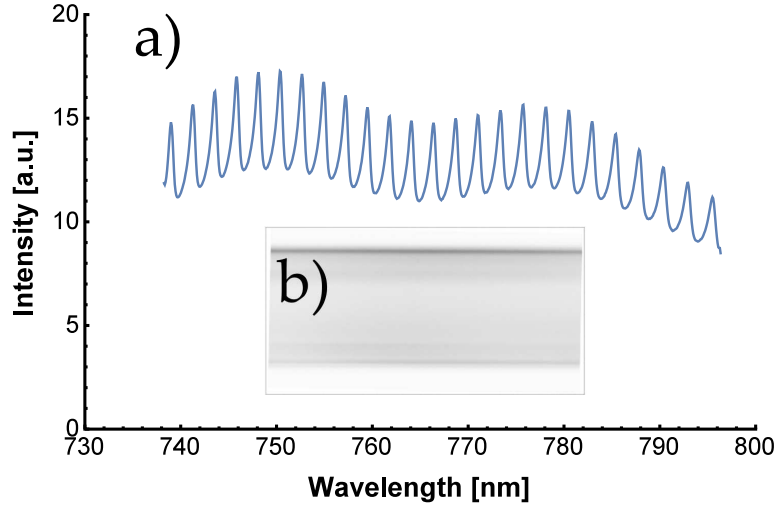
Figure 4.6: (a) TM-polarized fluorescence spectrum from an FCM with water in the channel. The capillary was oriented parallel to the entrance slit and the spectrum was vertically binned. (b) A fluorescence image of the channel region. The image intensity is from the fluorescence of the QDs that coat the channel wall. The nominal channel diameter is 50 μm.

the WGM spectra to be projected onto the full 2D CCD.

The capillary studied in this thesis was quite uniform along its length and showed a well-developed fluorescence WGM structure (Fig. 4.6). (The fabrication methods were discussed in detail in Chapter 2.2.3 and 2.3.3.) Here, the visibility, Q-factor, and free spectral range were 0.15, ~ 1300, and 2.5 nm respectively. Generally, the QD film was smoother along the length of the capillary as compared to the QD-coated fiber discussed in the previous section.

One problem with as-prepared capillaries is that the sensitivity does tend to be rather low, since fairly little of the mode field extends into the channel region [86]. This is because the deposited QD films tend to be thick, limiting the fraction of the resonant WGM field that samples the channel fluid. In order to deal with this issue and thereby improve the LoD, a set of numerical calculations were conducted in order to determine the optimal QD layer thickness needed to obtain the highest sensitivity. Once this was determined, we aimed to etch the QD film inside the capillary until the sensitivity was near the theoretical maximum.

The mode field equations derived in Chapter 1.2.2 were used to calculate the electric field profiles and refractometric sensitivities. For example, Fig. 4.7 shows the TM field intensity profile for the $l = 308$ and $n = 1$ cylindrical WGMs calculated from the TM component
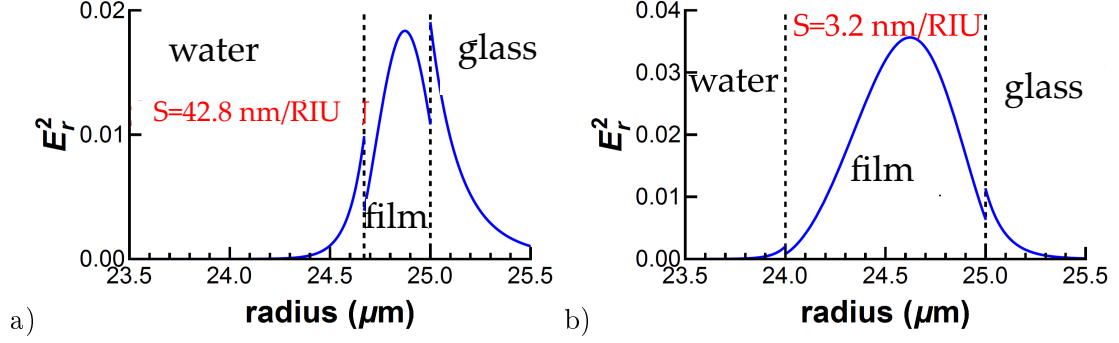
Figure 4.7: Calculated mode intensity profiles for a 50-μm-diameter capillary with QD layer thicknesses of 0.33 μm (a) and 1.0 μm (b). These are both first-order radial modes with an angular number $l = 308$. The thicker film has very little of the energy in the water and therefore has a low sensitivity of 3.2 nm/RIU.

of Eq. 1.32, for a capillary with a channel diameter of 50 μm and QD layer thicknesses of 0.33 μm and 1.00 μm, respectively. The discontinuities at the two interfaces are consistent with the boundary conditions associated with the TM polarization. For the thinner film, it is readily apparent that much more of the field profile extends into the channel region. The corresponding sensitivities were 41.7 nm/RIU and 3.1 nm/RIU respectively (using the cylindrical analogue of Eq. 1.51 from [161]), again consistent with the important effect of the QD layer thickness on the overall refractometric sensitivity.

In order to complete the picture, the sensitivities and Q-factors were plotted for QD layer thicknesses ranging from 0.15 to 1.0 μm (Fig. 4.8 and 4.9). The sensitivity was strongly dependent on the channel medium, as expected. Effectively, a higher-index medium "pulls" more of the field into the channel region and increases the sensitivity. More subtly, the thickness corresponding to the peak sensitivity also showed a dependence on the channel medium, with slightly thinner films being more optimal as the refractive index of the channel medium is increased. For water in the channel, the optimum thickness was found to be 0.33 μm, so this was set as a target for the etching procedure.

The calculated Q-factors also show a strong thickness dependence; for very thin QD layers the Q-factor approaches zero as the field confinement is lost. For thick films, the Q-factor reaches a constant value that is limited by absorption and scattering in the QDs (Fig. 4.9). While the Fourier shift method is not particularly sensitive to the Q-factor, it is interesting to note that there is also a QD layer thickness at which the Q-factor is
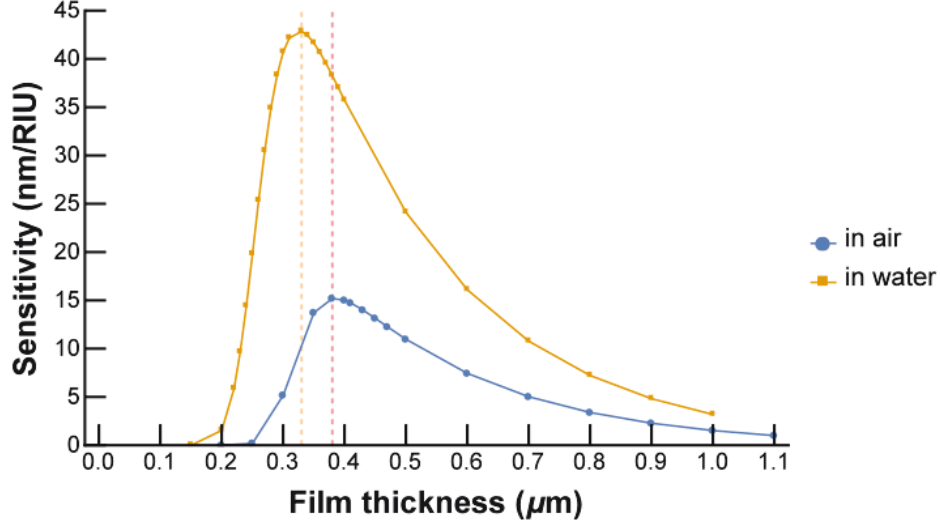
Figure 4.8: Calculated sensitivities for a 50-μm-diameter capillary, for different QD coating thicknesses. The points represent solutions to Eq. 1.32 for the first-order radial modes with l = 308 and a TM polarization. The orange and red vertical dashed lines correspond to the peak sensitivity values for water and air, respectively. The lines through the data are guides to the eye.

maximized. The reason for this behaviour is that the part of the mode not within the QD layer experiences no absorption and scattering loss, so one gets a trade-off between better confinement in the QD layer *vs.* absorption and scattering in that layer.

The sensitivity of the fluorescent capillary device was measured using standard methods. Essentially, a sequence of water-ethanol-water was pumped through the channel and the WGM shifts monitored as usual with vertical binning (Fig. 4.10 a). In the as-prepared device, the sensitivity was determined to be 6.5 nm/RIU, which is typical for structures of this type [86]. The theory plotted in (Fig. 4.8) predicted a sensitivity of 6.5 nm/RIU for thicknesses of either 0.22 μm or 0.80 μm. The thinner one was judged to be unlikely given that a very low Q-factor would also be expected (Fig. 4.9), but the observations gave significantly higher values closer to 1000. Thus, we conclude that the QD layer is on the "thick side" of the optimum sensitivity curve near 0.80 μm.

The QD layer thicknesses cannot be well controlled in the fabrication stage [87]. Therefore, in this work an etching procedure was used to thin the QD layer after the fabrication step. The procedure consisted of attaching the fluorescent capillary to the tubing as for standard measurement runs, and then pumping a solution of 10.0 M NaOH through the
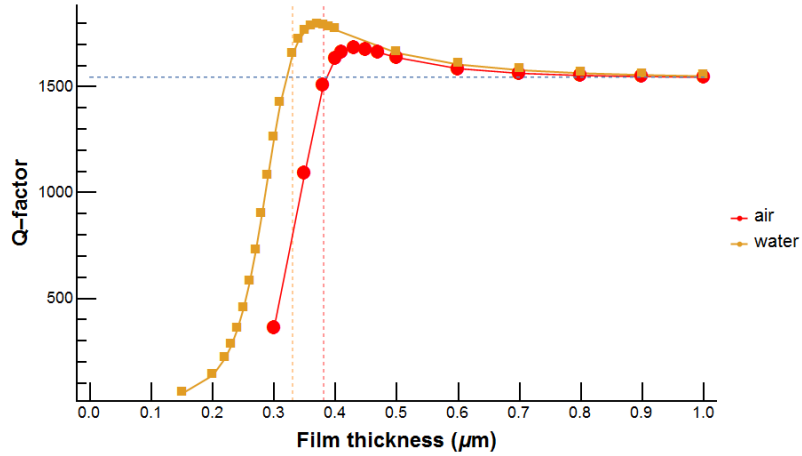
Figure 4.9: Calculated Q-factors for a 50-μm-diameter capillary, for different QD coating thicknesses. The points represent solutions to Eq. 1.32 for the first-order radial modes with l = 308 and a TM polarization, calculated using Eq. 1.27 where k is the resonant wavevector. The colored solid lines are guides to the eye. The green and red vertical dashed lines correspond to the peak sensitivities for water and air, respectively.

channel. NaOH is known to slowly etch silicon and silica glass [162] and may therefore remove the QD layer which consists of silicon QDs embedded in a glassy SiO_x matrix.

The etching process was monitored as follows. Initially, NaOH was pumped for 4 hours, then left overnight ($\sim$ 18 hours). Then a sensitivity measurement was performed as described in Chapter 2.6 and the sensitivity was determined before the next round of etching. This procedure was repeated 5 times. When the sensitivity reached 22 nm/RIU, then NaOH was pumped for 2 hours without leaving it overnight and the sensitivity measured between etches. This procedure was repeated 4 times, until the sensitivity started to drop instead of increase, which implied that the sensitivity had passed its peak (Fig. 4.11).

At this point, we had a fluorescent-core microcapillary with an excellent sensitivity of 28 nm/RIU. The peak sensitivity prior to the final etching step was 32 nm/RIU. This is among the highest reported for this type of structure [86, 87, 89, 159]. The 3σ shift resolution was next estimated from the scatter of the points in the "flat" part of the sensorgram (Fig. 4.10), yielding R = 3 pm.

In order to test this result, we next attempted a measurement in which the refractive index change of the channel medium would be close to the theoretical LoD. This was achieved
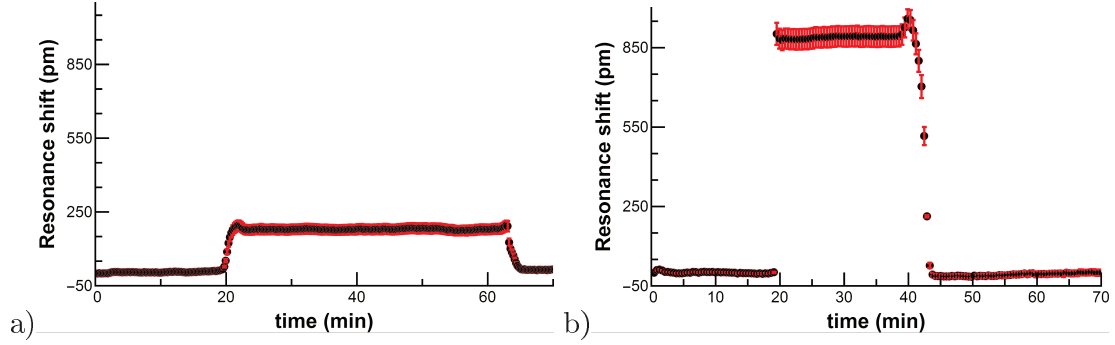
Figure 4.10: Sensorgrams of the water to ethanol to water transitions a) before etching and b) after etching close to the optimum film thickness in the FCM.
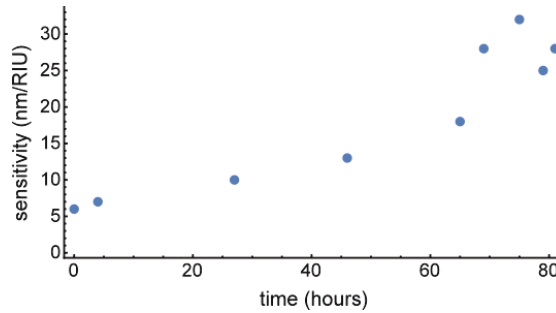
Figure 4.11: Measured sensitivity as a function of hours of etching.

by pumping, in order, solutions of 85.00%, 78.55%, and 85.00% ethanol in water by weight. The index of the mixture was calculated according to the method described in Chapter 2.6, so at a wavelength of 589 nm the corresponding index changed from 1.36556 to 1.36573, giving ΔRIU$=\sim 1.7 \times 10^{-4}$ RIU. The fluids were pre-injected into the capillary and all of the experimental precautions described earlier for reducing mechanical drift were utilized. The full vertical binning method was also employed in order to maximize the SNR.

The resulting sensorgram indicated that this shift was readily detected (Fig. 4.12), using two Fourier components in the shift analysis. There was a steady background drift so this was corrected *via* a linear background correction. The redshift of the WGM wavelengths was clearly observable and was quite close to the 3σ LoD for this device. To our knowledge, this is among the smallest experimentally measured refractive index change for a fluorescent-WGM-type device. The work also suggests means by which the LoD could be further improved; for example, the SNR would be further lowered by taking longer exposures than the 10 second ones employed here, although at the cost of increased analysis time and a

higher "disaster probability".

We finally wish to point out that other types of devices can certainly achieve higher sensitivities than we report here [57, 88, 163, 63, 28, 164, 83, 165]. Some of the highest values ever reported are for filled photonic crystal fibers, in which the reported sensitivity was 30 100 nm/RIU [52]. However, all of these devices have some advantages and disadvantages. Some require very high-index analytes [163] and such as the photonic crystal fiber mentioned above [52]. Others require expensive equipment and feature extremely fragile devices [88]. Still others, for example surface plasmon devices [57], cannot easily be integrated into capillary-type structures which have many advantages for microfluidic analyses. Thus we feel that it is important to determine the ultimate limit of each type of structure, because each one features different benefits and limitations and they are not strictly interchangeable.
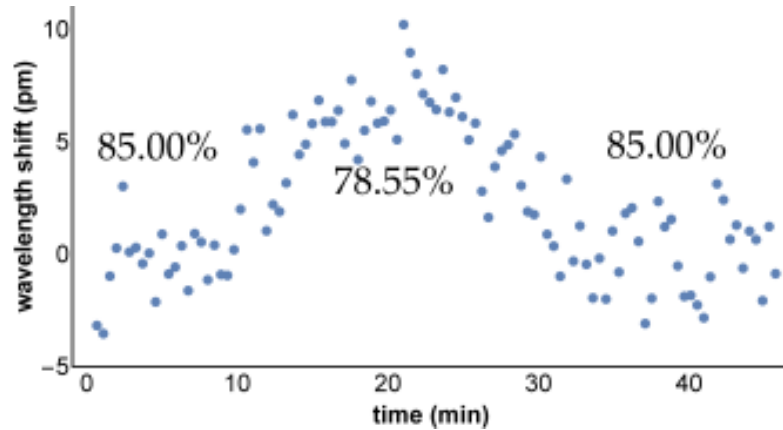
Figure 4.12: Sensorgram of varying concentrations of ethanol in water by weight, corresponding to a refractive index change of ΔRIU$=\sim 1.7 \times 10^{-4}$. The corresponding wavelength shift is ~ 5 pm. This sensorgram was achieved as follows: 10-second spectral images were collected as the solutions were pumped through the capillary. They were vertically binned and the Fourier shift theorem was applied to calculate the wavelength shifts, using the 3 strongest Fourier components. A slight background drift was corrected via a linear fit to the overall drift. The overall shift is close to the 3σ resolution.

Chapter 5

Conclusions

Optical microcavities can be used to control the luminescence spectrum and dynamics of ensembles of emitters such as luminescent quantum dots. Materials systems comprised of cavity-coupled QDs are, in fact, interesting both from the perspective of basic physics and for potential device applications. This thesis explored a sampling of both of these aspects, as related specifically to silicon-QDs deposited onto spherical or cylindrical microcavities.

The first part of this work explored the possibility of observing the Purcell effect in ensembles of Si-QDs coupled to an optical microsphere. To investigate this, a QD-coated microsphere was fabricated and the decay dynamics of the ensemble luminescence was investigated using a fluorescence lifetime imaging setup that was constructed as part of this project. This apparatus permits one to create a dynamic "movie" with (in this case) one-microsecond frames that allow one to spatially map the decay dynamics.

While the emission spectrum could not, at the time, be readily measured, it was felt that the overall decay dynamics might show certain effects if the QD ensemble was well coupled to the whispering gallery modes of the microsphere. These effects should be measurable on the basis of the decay parameters associated with the commonly-used stretched exponential luminescence decay. While pronounced WGM oscillations were observed in the QD luminescence spectrum, there were no consistent variations in the luminescence lifetimes in parts of the sphere showing strong WGMs (typically around the equator) as compared to other regions that did not.

The negative result is believed to have many possible origins. For example, the nonradiative decay rate, which is not affected by Purcell-type rate enhancements or suppressions,

may be too large in these Si-QDs. Alternatively, there may be too much background luminescence from uncoupled QDs and, indeed, the WGM visibility was not especially high in the samples investigated here. Perhaps in retrospect it was too optimistic to expect to observe Purcell effects, but the work did suggest means to observe such effects in the future. Perhaps most important is to improve the quantum efficiency, which is in fact a direction currently being explored by our collaborators, who have demonstrated "freestanding" Si-QDs with efficiencies above 60% [166]. The ability to do spectrally resolved lifetime imaging would also be important, but the signal intensities are currently too low.

The next step of this project was to explore the refractive index sensing capacity of structures similar to those investigated for Purcell enhancements. This work used cylindrical cavities rather than spherical ones, mainly for reasons of convenience. The aim was to see how low the limits of detection can be pushed, using fluorescence-based microcavity measurements. To achieve this, liquids were flowed around QD-coated optical fibers or through coated capillaries, while the fluorescence WGM spectrum was carefully monitored.

In this part of the project, both optical fibers and microcapillaries were investigated. One of the main advantages of such structures is that they can be aligned with the entrance slit of a spectrometer such that the WGMs "align" vertically on a 2D CCD array, which, by vertical binning, significantly improves the signal-to-noise ratio as compared to standard linear CCDs. In addition to this enhancement, a range of experimental improvements were developed to minimize noise and drift in the WGM spectral data over time.

Microcapillaries turned out to be more stable than optical fibers, which suffered from significant mechanical instabilities due to our inability to stabilize them sufficiently as the fluid flowed past. In contrast, capillaries did not suffer nearly as severely from this effect. However, air motions in the lab, possible laser heating, and especially mechanical vibrations associated with opening and closing fluidic valves attached to the tubing were found to be severe problems. These difficulties were minimized using a number of techniques, such as minimizing the laser power as much as reasonably possible, pre-filling the tubes with the various solutions, and covering the entire apparatus with a foil enclosure.

In the end, we were able to demonstrate a limit of detection for a fluorescent microcapillary-type refractometric sensor of $\sim 1.7 \times 10^{-4}$ RIU, which is less than a factor of 2 larger than

the calculated optimum theoretical LoD. While such detection limits are not particularly impressive in comparison to some other technologies, it is to our knowledge the best one actually measured for fluorescent WGM-type sensors. In addition, the expensive and fragile apparatus typical of other WGM-type sensing structures is completely avoided. It should be noted that these measurements involve a 5-picometer spectral shift, which is resolved on a standard miniature spectrograph system. Since we are clearly pushing the ultimate limits of this device, further improvements may require achieving a better SNR, a higher refractometric sensitivity, or improving the wavelength resolution of the system, although the latter admittedly comes at additional costs. The work may also have implications for other measurements in which very tiny shifts of a periodic emission spectrum need to be determined with a relatively inexpensive measurement system.

Bibliography

[1] B. J. Luff, J. S. Wilkinson, J. Piehler, U. Hollenbach, J. Ingenhoff, and N. Fabricius, "Integrated optical Mach-Zehnder biosensor," Journal of Lightwave Technology **16**, 583–592 (1998).

[2] K. Schmitt, B. Schirmer, C. Hoffmann, A. Brandenburg, and P. Meyrueis, "Interferometric biosensor based on planar optical waveguide sensor chips for label-free detection of surface bound bioreactions," Biosensors and Bioelectronics **22**, 2591–2597 (2007).

[3] M. G. Scullion, a. Di Falco, and T. F. Krauss, "Slotted photonic crystal cavities with integrated microfluidics for biosensing applications," Biosensors and Bioelectronics **27**, 101–105 (2011).

[4] M. Li, S. K. Cushing, and N. Wu, "Plasmon-enhanced optical sensors: a review," The Analyst **140**, 386–406 (2015).

[5] A. V. Kabashin, S. Patskovsky, and A. N. Grigorenko, "Phase and amplitude sensitivities in surface plasmon resonance bio and chemical sensing." Optics express **17**, 21191–21204 (2009).

[6] F. Vollmer and S. Arnold, "Whispering-gallery-mode biosensing: label-free detection down to single molecules." Nature methods **5**, 591–596 (2008).

[7] Y. Zhi, "Whispering gallery modes in layered microspheres: mode structure, thermal response, and reactive sensing," Phd thesis, University of Alberta (2014).

[8] C. M. Hessel, E. J. Henderson, and J. G. C. Veinot, "Hydrogen silsesquioxane: A molecular precursor for nanocrystalline Si-SiO2 composites and freestanding hydride-

surface-terminated silicon nanoparticles," Chemistry of Materials **18**, 6139–6146 (2006).

[9] D. R. Lide, ed., *CRC Handbook of Chemistry and Physics, 85th Edition* (CRC Press, 2004).

[10] C.-y. Chao, T. Ling, and L. J. Guo, "Label-Free Biochemical Sensors Based on Optical Microresonators," in "Sensors (Peterborough, NH)," , X. Fan, ed. (Springer New York, 2009), chap. 8, pp. 177–227.

[11] S. J. Mihailov, "Fiber bragg grating sensors for harsh environments," Sensors **12**, 1898–1918 (2012).

[12] R. Heideman and P. Lambeck, "Remote opto-chemical sensing with extreme sensitivity: design, fabrication and performance of a pigtailed integrated optical phase-modulated Mach-Zehnder interferometer system," Sensors and Actuators B: Chemical **61**, 100–127 (1999).

[13] D. Erickson, S. Mandal, A. H. J. Yang, and B. Cordovez, "Nanobiosensors: optofluidic, electrical and mechanical approaches to biomolecular detection at the nanoscale." Microfluidics and nanofluidics **4**, 33–52 (2008).

[14] U. Resch-Genger, M. Grabolle, S. Cavaliere-Jaricot, R. Nitschke, and T. Nann, "Quantum dots versus organic dyes as fluorescent labels." Nature methods **5**, 763–75 (2008).

[15] I. L. Medintz, H. T. Uyeda, E. R. Goldman, and H. Mattoussi, "Quantum dot bioconjugates for imaging, labelling and sensing." Nature materials **4**, 435–46 (2005).

[16] M. L. Brongersma, P. G. Kik, A. Polman, K. S. Min, and H. A. Atwater, "Size-dependent electron-hole exchange interaction in Si nanocrystals," Applied Physics Letters **76**, 351 (2000).

[17] X. Fan, I. M. White, S. I. Shopova, H. Zhu, J. D. Suter, and Y. Sun, "Sensitive optical biosensors for unlabeled targets: a review." Analytica chimica acta **620**, 8–26 (2008).

[18] J. Knittel, J. D. Swaim, and W. P. Bowen, "Whispering gallery mode biosensors with plasmonic enhancement," SPIE Newsroom pp. 2–4 (2012).

[19] S. I. Shopova, R. Rajmangal, S. Holler, and S. Arnold, "Plasmonic enhancement of a whispering-gallery-mode biosensor for single nanoparticle detection," Applied Physics Letters **98**, 243104 (2011).

[20] A. K. Sharma, R. Jha, and B. D. Gupta, "Fiber-optic sensors based on surface plasmon resonance: A comprehensive review," IEEE Sensors Journal **7**, 1118–1129 (2007).

[21] S. Arnold, V. R. Dantham, C. Barbre, B. a. Garetz, and X. Fan, "Periodic plasmonic enhancing epitopes on a whispering gallery mode biosensor." Optics express **20**, 26147–59 (2012).

[22] B. H. Schneider, J. G. Edwards, and N. F. Hartman, "Hartman interferometer: Versatile integrated optic sensor for label- free, real-time quantification of nucleic acids, proteins, and pathogens," Clinical Chemistry **43**, 1757–1763 (1997).

[23] M. Zourob, S. Elwary, and A. Turner, eds., *Principles of Bacterial Detection: Biosensors, Recognition Receptors and Microsystems* (Springer New York, New York, NY, 2008).

[24] D. P. Campbell, *Principles of Bacterial Detection: Biosensors, Recognition Receptors and Microsystems* (Springer New York, New York, NY, 2008).

[25] B. Sepulveda, J. S. del Rio, M. Moreno, F. J. Blanco, K. Mayora, C. Domínguez, and L. M. Lechuga, "Optical biosensor microsystems based on the integration of highly sensitive Mach-Zehnder interferometer devices," Journal of Optics A: Pure and Applied Optics **8**, S561–S566 (2006).

[26] S. Dante, D. Duval, B. Sepúlveda, A. B. González-Guerrero, J. R. Sendra, and L. M. Lechuga, "All-optical phase modulation for integrated interferometric biosensors," Optics Express **20**, 7195 (2012).

[27] H. Wang, X. Lan, J. Huang, L. Yuan, C.-W. Kim, and H. Xiao, "Fiber pigtailed thin wall capillary coupler for excitation of microsphere WGM resonator," Opt. Express **21**, 15834–15839 (2013).

[28] N. Lin, L. Jiang, S. Wang, H. Xiao, Y. Lu, and H.-L. Tsai, "Design and optimization of liquid core optical ring resonator for refractive index sensing." Applied optics **50**, 3615–3621 (2011).

[29] H. Wu, H. Huang, M. Bai, P. Liu, M. Chao, J. Hu, J. Hao, and T. Cao, "An ultra-low detection-limit optofluidic biosensor based on all glass Fabry-Perot cavity," Optics Express **22**, 31977 (2014).

[30] J. M. Weissman, H. B. Sunkara, A. S. Tse, and S. A. Asher, "Thermally Switchable Periodicities and Diffraction from Mesoscopically Ordered Materials," Science **274**, 959–963 (1996).

[31] M. C. Chiappelli and R. C. Hayward, "Photonic multilayer sensors from photo-crosslinkable polymer films." Advanced materials (Deerfield Beach, Fla.) **24**, 6100–4 (2012).

[32] I. Pavlichenko, A. T. Exner, M. Guehl, P. Lugli, G. Scarpa, and B. V. Lotsch, "Humidity-Enhanced Thermally Tunable TiO 2 /SiO 2 Bragg Stacks," The Journal of Physical Chemistry C **116**, 298–305 (2012).

[33] M. M. Hawkeye and M. J. Brett, "Optimized Colorimetric Photonic-Crystal Humidity Sensor Fabricated Using Glancing Angle Deposition," Advanced Functional Materials **21**, 3652–3658 (2011).

[34] A. C. Arsenault, T. J. Clark, G. von Freymann, L. Cademartiri, R. Sapienza, J. Bertolotti, E. Vekris, S. Wong, V. Kitaev, I. Manners, R. Z. Wang, S. John, D. Wiersma, and G. A. Ozin, "From colour fingerprinting to the control of photo-luminescence in elastic photonic crystals," Nature Materials **5**, 179–184 (2006).

[35] J. Li, Y. Wu, J. Fu, Y. Cong, J. Peng, and Y. Han, "Reversibly strain-tunable elas-tomeric photonic crystals," Chemical Physics Letters **390**, 285–289 (2004).

[36] T. Chen, Z. Han, J. Liu, and Z. Hong, "Terahertz gas sensing based on a simple one-dimensional photonic crystal cavity with high-quality factors," Applied Optics **53**, 3454 (2014).

[37] S. Olyaee, A. Naraghi, and V. Ahmadi, "High sensitivity evanescent-field gas sensor based on modified photonic crystal fiber for gas condensate and air pollution monitoring," Optik - International Journal for Light and Electron Optics **125**, 596–600 (2014).

[38] Y. Zou, S. Chakravarty, W.-C. Lai, C.-Y. Lin, and R. T. Chen, "Methods to array photonic crystal microcavities for high throughput high sensitivity biosensing on a silicon-chip based platform," Lab on a Chip **12**, 2309 (2012).

[39] C. Fenzl, T. Hirsch, and O. S. Wolfbeis, "Photonic crystals for chemical sensing and biosensing," Angewandte Chemie - International Edition **53**, 3318–3335 (2014).

[40] B. Troia, A. Paolicelli, F. D. Leonardis, and V. M. N. Passaro, "Photonic Crystals for Optical Sensing : A Review," in "Advances in Photonic Crystals," (2013), pp. 241–295.

[41] J. Jágerská, H. Zhang, Z. Diao, N. Le Thomas, and R. Houdré, "Refractive index sensing with an air-slot photonic crystal nanocavity." Optics letters **35**, 2523–2525 (2010).

[42] V. Toccafondo, J. García-Rupérez, M. J. Bañuls, a. Griol, J. G. Castelló, S. Peransi-Llopis, and a. Maquieira, "Single-strand DNA detection using a planar photonic-crystal-waveguide-based sensor." Optics letters **35**, 3673–3675 (2010).

[43] S. Zlatanovic, L. W. Mirkarimi, M. M. Sigalas, M. a. Bynum, E. Chow, K. M. Robotti, G. W. Burr, S. Esener, and A. Grot, "Photonic crystal microcavity sensor for ultracompact monitoring of reaction kinetics and protein concentration," Sensors and Actuators, B: Chemical **141**, 13–19 (2009).

[44] H. Clevenson, P. Desjardins, X. Gan, and D. Englund, "High sensitivity gas sensor based on high-Q suspended polymer photonic crystal nanocavity," Applied Physics Letters **104**, 241108 (2014).

[45] A. M. R. Pinto and M. Lopez-Amo, "Photonic Crystal Fibers for Sensing Applications," Journal of Sensors **2012**, 1–21 (2012).

[46] H. Ding, X. Li, J. Cui, L. Yang, and S. Dong, "AN ALL-FIBER GAS SENSING SYS-
TEM USING HOLLOW-CORE PHOTONIC BANDGAP FIBER AS GAS CELL,"
Instrumentation Science & Technology **39**, 78–87 (2011).

[47] V. P. Minkovich, D. Monzón-Hernández, J. Villatoro, and G. Badenes, "Microstruc-
tured optical fiber coated with thin films for gas and chemical sensing," Optics Express
14, 8413 (2006).

[48] L. Zou, X. Bao, S. Afshar V., and L. Chen, "Dependence of the Brillouin frequency
shift on strain and temperature in a photonic crystal fiber," Optics Letters **29**, 1485
(2004).

[49] Y.-G. Han, Y. Chung, S. B. Lee, C.-S. Kim, M. Y. Jeong, and M. K. Kim, "Tem-
perature and strain discrimination based on a temperature-insensitive birefringent
interferometer incorporating an erbium-doped fiber," Applied Optics **48**, 2303 (2009).

[50] T. M. Monro, S. Warren-Smith, E. P. Schartner, A. François, S. Heng, H. Ebendorff-
Heidepriem, and S. Afshar, "Sensing with suspended-core optical fibers," Optical Fiber
Technology **16**, 343–356 (2010).

[51] H. Qu and M. Skorobogatiy, "Liquid-core low-refractive-index-contrast Bragg fiber
sensor," Applied Physics Letters **98**, 201114 (2011).

[52] D. K. C. Wu, B. T. Kuhlmey, and B. J. Eggleton, "Ultrasensitive photonic crystal
fiber refractive index sensor," Optics Letters **34**, 322 (2009).

[53] a. François, K. J. Rowland, T. Reynolds, S. J. Nicholls, and T. M. Monro, "Combining
whispering gallery mode lasers and microstructured optical fibers for in-vivo biosensing
applications," **8915**, 891518 (2013).

[54] J. Homola, S. S. Yee, and G. Gauglitz, "Surface plasmon resonance sensors: review,"
Sensors and Actuators B: Chemical **54**, 3–15 (1999).

[55] P. Preechaburana, M. C. Gonzalez, A. Suska, and D. Filippini, "Surface plasmon res-
onance chemical sensing on cell phones," Angewandte Chemie - International Edition
51, 11585–11588 (2012).

[56] K. Bremer and B. Roth, "Fibre optic surface plasmon resonance sensor system designed for smartphones." Optics express **23**, 17179–84 (2015).

[57] J. Homola, ed., *Surface Plasmon Resonance Based Sensors*, vol. 4 of *Springer Series on Chemical Sensors and Biosensors* (Springer Berlin Heidelberg, Berlin, Heidelberg, 2006).

[58] O. Lazcka, F. J. Del Campo, and F. X. Muñoz, "Pathogen detection: a perspective of traditional methods and biosensors." Biosensors & bioelectronics **22**, 1205–17 (2007).

[59] B. E. a. Saleh and M. C. Teich, "Fundamentals of Photonics , 2nd Edition," World (1997).

[60] K. a. Willets and R. P. Van Duyne, "Localized surface plasmon resonance spectroscopy and sensing." Annual review of physical chemistry **58**, 267–97 (2007).

[61] S. L. Kleinman, E. Ringe, N. Valley, K. L. Wustholz, E. Phillips, K. A. Scheidt, G. C. Schatz, and R. P. Van Duyne, "Single-molecule surface-enhanced Raman spectroscopy of crystal violet isotopologues: theory and experiment." Journal of the American Chemical Society **133**, 4115–22 (2011).

[62] D. X. Xu, a. Densmore, a. Delâge, P. Waldron, R. McKinnon, S. Janz, J. Lapointe, G. Lopinski, T. Mischki, E. Post, P. Cheben, and J. H. Schmid, "Folded cavity SOI microring sensors for high sensitivity and real time measurement of biomolecular binding." Optics express **16**, 15137–15148 (2008).

[63] T. Claes, J. Molera, K. De Vos, E. Schacht, R. Baets, and P. Bienstman, "Label-Free Biosensing With a Slot-Waveguide-Based Ring Resonator in Silicon on Insulator," IEEE Photonics Journal **1**, 197–204 (2009).

[64] K. B. Gylfason, C. F. Carlborg, A. Kaźmierczak, F. Dortu, H. Sohlström, L. Vivien, C. A. Barrios, W. van der Wijngaart, and G. Stemme, "On-chip temperature compensation in an integrated slot-waveguide ring resonator refractive index sensor array." Optics express **18**, 3226–37 (2010).

[65] C. F. Carlborg, K. B. Gylfason, A. Kaźmierczak, F. Dortu, M. J. Bañuls Polo, A. Maquieira Catala, G. M. Kresbach, H. Sohlström, T. Moh, L. Vivien, J. Popplewell, G. Ronan, C. A. Barrios, G. Stemme, and W. van der Wijngaart, "A packaged optical slot-waveguide ring resonator sensor array for multiplex label-free assays in labs-on-chips." Lab on a chip **10**, 281–90 (2010).

[66] C. A. Barrios, K. B. Gylfason, B. Sánchez, A. Griol, H. Sohlström, M. Holgado, and R. Casquel, "Slot-waveguide biochemical sensor," Optics Letters **32**, 3080 (2007).

[67] D. Marazuela and M. C. Moreno-Bondi, "Fiber-optic biosensors–an overview." Analytical and bioanalytical chemistry **372**, 664–82 (2002).

[68] K. H. Smith, B. L. Ipson, T. L. Lowder, A. R. Hawkins, R. H. Selfridge, and S. M. Schultz, "Surface-relief fiber Bragg gratings for sensing applications," Applied Optics **45**, 1669 (2006).

[69] P. E. Henning and P. Geissinger, "Application of time-correlated single photon counting and stroboscopic detection methods with an evanescent-wave fibre-optic sensor for fluorescence-lifetime-based pH measurements," Measurement Science and Technology **23**, 045104 (2012).

[70] C. Chiang, J. Chao, and C. Chien, "Optical fiber concentration sensor based on whispering gallery mode interference," in "Innovation, Communication . . . ," (2013), pp. 365–368.

[71] Z. Zhang, R. Lockwood, J. Veinot, and a. Meldrum, "Detection of ethanol and water vapor with silicon quantum dots coupled to an optical fiber," Sensors and Actuators B: Chemical **181**, 523–528 (2013).

[72] T. L. Lowder, J. D. Gordon, S. M. Schultz, and R. H. Selfridge, "Volatile organic compound sensing using a surface-relief D-shaped fiber Bragg grating and a poly-dimethylsiloxane layer," Optics Letters **32**, 2523 (2007).

[73] J.-l. Kou, J. Feng, L. Ye, F. Xu, and Y.-q. Lu, "Miniaturized fiber taper reflective interferometer for high temperature measurement." Optics express **18**, 14245–14250 (2010).

[74] A. Majumdar and H. Huang, "Development of an in-fiber white-light interferometric distance sensor for absolute measurement of arbitrary small distances." Applied optics **47**, 2821–2828 (2008).

[75] R. S. Brown, I. Kozin, Z. Tong, R. D. Oleschuk, and H.-P. Loock, "Fiber-loop ringdown spectroscopy," The Journal of Chemical Physics **117**, 10444 (2002).

[76] Z. Tong, M. Jakubinek, A. Wright, A. Gillies, and H.-P. Loock, "Fiber-loop ring-down spectroscopy: A sensitive absorption technique for small liquid samples," Review of Scientific Instruments **74**, 4818 (2003).

[77] A. Chryssis, S. Saini, S. Lee, W. Bentley, and M. Dagenais, "Detecting hybridization of DNA by highly sensitive evanescent field etched core fiber Bragg grating sensors," IEEE Journal of Selected Topics in Quantum Electronics **11**, 864–872 (2005).

[78] L. Rayleigh, "The problem of the whispering gallery," Philosophical Magazine Series 6 **20**, 1001–1004 (1910).

[79] L. Rayleigh, "IX. Further applications of Bessel's functions of high order to the Whispering Gallery and allied problems," Philosophical Magazine Series 6 **27**, 100–109 (1914).

[80] J. Dutka, "On the early history of Bessel functions," Archive for History of Exact Sciences **49**, 105–134 (1995).

[81] S. Soria, S. Berneschi, M. Brenci, F. Cosi, G. N. Conti, S. Pelli, and G. C. Righini, "Optical microspherical resonators for biomedical sensing," Sensors **11**, 785–805 (2011).

[82] F. Vollmer, D. Braun, a. Libchaber, M. Khoshsima, I. Teraoka, and S. Arnold, "Protein detection by optical shift of a resonant microcavity," Applied Physics Letters **80**, 4057–4059 (2002).

[83] Y. Zhi, T. Thiessen, and A. Meldrum, "Silicon quantum dot coated microspheres for microfluidic refractive index sensing," Journal of the Optical Society of America B **30**, 51 (2012).

[84] A. M. Armani, R. P. Kulkarni, S. E. Fraser, R. C. Flagan, and K. J. Vahala, "Label-free, single-molecule detection with optical microcavities." Science (New York, N.Y.) **317**, 783–787 (2007).

[85] E. Krioukov, J. Greve, and C. Otto, "Performance of integrated optical microcavities for refractive index and fluorescence sensing," Sensors and Actuators B: Chemical **90**, 58–67 (2003).

[86] S. Lane, J. Chan, T. Thiessen, and a. Meldrum, "Whispering gallery mode structure and refractometric sensitivity of fluorescent capillary-type sensors," Sensors and Actuators, B: Chemical **190**, 752–759 (2014).

[87] C. P. K. Manchee, V. Zamora, J. W. Silverstone, J. G. C. Veinot, and a. Meldrum, "Refractometric sensing with fluorescent-core microcapillaries," (2011).

[88] I. M. White, H. Oveys, and X. Fan, "Liquid-core optical ring-resonator sensors." Optics letters **31**, 1319–1321 (2006).

[89] P. Bianucci, J. R. Rodriguez, C. M. Clements, J. G. C. Veinot, and A. Meldrum, "Silicon nanocrystal luminescence coupled to whispering gallery modes in optical fibers," Journal of Applied Physics **105**, 023108 (2009).

[90] A. Boleininger, T. Lake, S. Hami, and C. Vallance, "Whispering gallery modes in standard optical fibres for fibre profiling measurements and sensing of unlabelled chemical species," Sensors **10**, 1765–1781 (2010).

[91] T. L. Chow, *Mathematical Methods for Physicists: A Concise Introduction* (Cambridge University Press, 2000).

[92] I. Teraoka, S. Arnold, and F. Vollmer, "Perturbation approach to resonance shifts of whispering-gallery modes in a dielectric microsphere as a probe of a surrounding medium," (2003).

[93] I. Teraoka and S. Arnold, "Whispering-gallery modes in a microsphere coated with a high-refractive index layer: polarization-dependent sensitivity enhancement of the resonance-shift sensor and TE-TM resonance matching," (2007).

[94] I. Teraoka and S. Arnold, "Enhancing the sensitivity of a whispering-gallery mode microsphere sensor by a high-refractive-index surface layer," Journal of the Optical Society of America B **23**, 1434 (2006).

[95] I. Teraoka, S. Arnold, and F. Vollmer, "Perturbation approach to resonance shifts of whispering-gallery modes in a dielectric microsphere as a probe of a surrounding medium," Journal of the Optical Society of America B **20**, 1937 (2003).

[96] B. R. Johnson, "Theory of morphology-dependent resonances: shape resonances and width formulas," Journal of the Optical Society of America A **10**, 343 (1993).

[97] M. Fox, *Quantum Optics: An Introduction*, vol. 67 (Oxford University Press, 2006).

[98] M. L. Gorodetsky, a. a. Savchenkov, and V. S. Ilchenko, "Ultimate Q of optical microsphere resonators." Optics letters **21**, 453–455 (1996).

[99] P. Bianucci, X. Wang, J. G. Veinot, and a. Meldrum, "Silicon nanocrystals on bottle resonators: mode structure, loss mechanisms and emission dynamics." Optics express **18**, 8466–81 (2010).

[100] Y. Zhi and A. Meldrum, "Tuning a microsphere whispering-gallery-mode sensor for extreme thermal stability," Applied Physics Letters **105**, 031902 (2014).

[101] R. D. Kekatpure and M. L. Brongersma, "Fundamental photophysics and optical loss processes in Si-nanocrystal-doped microdisk resonators," Physical Review A - Atomic, Molecular, and Optical Physics **78** (2008).

[102] O. Benson, S. Goetzinger, A. Mazzei, G. Zumofen, V. Sandoghdar, and L. d. S. Menezes, "Nanophotonics with microsphere resonators," in "VLSI Micro- and Nanophotonics," , E.-H. Lee, L. Eldada, M. Razeghi, and C. Jagadish, eds. (2010), chap. 5.

[103] A. Kavokin, J. J. Baumberg, G. Malpuech, and F. P. Laussy, *Microcavities* (OUP Oxford, 2007).

[104] I. H. Agha, J. E. Sharping, M. a. Foster, and a. L. Gaeta, "Optimal sizes of silica microspheres for linear and nonlinear optical interactions," Applied Physics B: Lasers and Optics **83**, 303–309 (2006).

[105] K. J. Vahala, "Optical microcavities." Nature **424**, 839–46 (2003).

[106] G. Khitrova, H. M. Gibbs, M. Kira, S. W. Koch, and A. Scherer, "Vacuum Rabi splitting in semiconductors," Nature Physics **2**, 81–90 (2006).

[107] X. Fan, M. Lonergan, Y. Zhang, and H. Wang, "Enhanced spontaneous emission from semiconductor nanocrystals embedded in whispering gallery optical microcavities," Physical Review B **64**, 115310 (2001).

[108] J. P. Reithmaier, G. Sek, A. Löffler, C. Hofmann, S. Kuhn, S. Reitzenstein, L. V. Keldysh, V. D. Kulakovskii, T. L. Reinecke, and A. Forchel, "Strong coupling in a single quantum dot-semiconductor microcavity system." Nature **432**, 197–200 (2004).

[109] N. L. Thomas, U. Woggon, and O. Schöps, "Cavity QED with semiconductor nanocrystals," Nano . . . **6**, 557–561 (2006).

[110] T. Hümmer, F. J. García-Vidal, L. Martín-Moreno, and D. Zueco, "Weak and strong coupling regimes in plasmonic QED," Physical Review B **87**, 115419 (2013).

[111] E. Purcell, "Spontaneous emission probabilities at radio frequencies," Physical Review **69**, 681 (1946).

[112] H. Yokoyama, Y. Nambu, and T. Kawakami, "Controlling spontaneous emission and optical microcavities," in "Confined Electrons and Photons: New Physics and Applications," , E. Burstein and C. Weisbuch, eds. (Plenum Press, New York, 1995), p. 427.

[113] a. Meldrum, P. Bianucci, and F. Marsiglio, "Modification of ensemble emission rates and luminescence spectra for inhomogeneously broadened distributions of quantum dots coupled to optical microcavities." Optics express **18**, 10230–46 (2010).

[114] J. Gérard, B. Sermage, B. Gayral, B. Legrand, E. Costard, and V. Thierry-Mieg, "Enhanced Spontaneous Emission by Quantum Boxes in a Monolithic Optical Microcavity," (1998).

[115] K.-S. Hsu, W.-C. Hung, C.-C. Chang, W.-H. Lin, M.-H. Shih, P.-T. Lee, S.-Y. Lin, S.-W. Chang, and Y.-C. Chang, "Lasing action and extraordinary reduction in long radiative lifetime of type-II GaSb/GaAs quantum dots using circular photonic crystal nanocavity," Applied Physics Letters **107**, 091113 (2015).

[116] M. V. Artemyev, U. Woggon, R. Wannemacher, H. Jaschinski, and W. Langbein, "Light Trapped in a Photonic Dot:Â Microspheres Act as a Cavity for Quantum Dot Emission," Nano Letters **1**, 309–314 (2001).

[117] a. Belarouci and F. Gourbilleau, "Microcavity enhanced spontaneous emission from silicon nanocrystals," Journal of Applied Physics **101**, 073108 (2007).

[118] S. Arnold, M. Khoshsima, I. Teraoka, S. Holler, and F. Vollmer, "Shift of whispering-gallery modes in microspheres by protein adsorption." Optics letters **28**, 272–274 (2003).

[119] F. Vollmer and S. Arnold, "Optical microcavities: single virus detection and nanoparticle trapping," in "SPIE NanoScience+ . . . ," , vol. 7397, M. Razeghi and H. Mohseni, eds. (International Society for Optics and Photonics, 2009), vol. 7397, pp. 739702–1–739702–9.

[120] I. M. White and X. Fan, "On the performance quantification of resonant refractive index sensors," Optics Express **16**, 1020 (2008).

[121] I. Teraoka and S. Arnold, "Theory of resonance shifts in TE and TM whispering gallery modes by nonradial perturbations for sensing applications," Journal of the Optical Society of America B **23**, 1381 (2006).

[122] H.-C. Ren, F. Vollmer, S. Arnold, and A. Libchaber, "High-Q microsphere biosensor - analysis for adsorption of rodlike bacteria." Optics express **15**, 17410–17423 (2007).

[123] A. François, T. Reynolds, and T. M. Monro, "A fiber-tip label-free biological sensing platform: a practical approach toward in-vivo sensing." Sensors (Basel, Switzerland) **15**, 1168–81 (2015).

[124] F. Vollmer and L. Yang, "Label-free detection with high-Q microcavities: a review of biosensing mechanisms for integrated devices," Nanophotonics Science Wise Publishing & De Gruyter @BULLET Berlin @BULLET Boston **1**, 267–291 (2012).

[125] I. Teraoka and S. Arnold, "Coupled whispering gallery modes in a multilayer-coated microsphere." Optics letters **32**, 1147–1149 (2007).

[126] W. von Klitzing, R. Long, V. S. Ilchenko, J. Hare, and V. Lefèvre-Seguin, "Tunable whispering gallery modes for spectroscopy and CQED experiments," New Journal of Physics **3** (2001).

[127] I. M. White, H. Oveys, X. Fan, T. L. Smith, and J. Zhang, "Integrated multiplexed biosensors based on liquid core optical ring resonators and antiresonant reflecting optical waveguides," Applied Physics Letters **89**, 191106 (2006).

[128] K. J. Rowland, A. François, P. Hoffmann, and T. M. Monro, "Fluorescent polymer coated capillaries as optofluidic refractometric sensors." Optics express **21**, 11492–505 (2013).

[129] J. Silverstone, S. McFarlane, C. Manchee, and a. Meldrum, "Ultimate resolution for refractometric sensing with whispering gallery mode microcavities," Optics Express **20**, 8284 (2012).

[130] C. M. Hessel, M. A. Summers, A. Meldrum, M. Malac, and J. G. C. Veinot, "Direct Patterning, Conformal Coating, and Erbium Doping of Luminescent nc-Si/SiO2 Thin Films from Solution Processable Hydrogen Silsesquioxane," Advanced Materials **19**, 3513–3516 (2007).

[131] S. P. Withrow, C. W. White, A. Meldrum, J. D. Budai, D. M. Hembree, and J. C. Barbour, "Effects of hydrogen in the annealing environment on photoluminescence from Si nanoparticles in SiO[sub 2]," Journal of Applied Physics **86**, 396 (1999).

[132] J. Narayan, P. Tiwari, X. Chen, J. Singh, R. Chowdhury, and T. Zheleva, "Epitaxial growth of TiN films on (100) silicon substrates by laser physical vapor deposition," Applied Physics Letters **61**, 1290 (1992).

[133] B. S. Meyerson, "Low-temperature silicon epitaxy by ultrahigh vacuum/chemical vapor deposition," Applied Physics Letters **48**, 797 (1986).

[134] T. Shimizu-Iwayama, M. Ohshima, T. Niimi, S. Nakao, K. Saitoh, T. Fujita, and N. Itoh, "Visible photoluminescence related to Si precipitates in Si + -implanted SiO 2," Journal of Physics: Condensed Matter **5**, L375–L380 (1993).

[135] A. Meldrum, R. F. J. Haglund, L. A. Boatner, and C. W. White, "Nanocomposite Materials Formed by Ion Implantation," Advanced Materials **13**, 1431–1444 (2001).

[136] J. Rheims, J. Köser, and T. Wriedt, "Refractive-index measurements in the near-IR using an Abbe refractometer," Measurement Science and Technology **8**, 601–605 (1997).

[137] X. Quan and E. S. Fry, "Empirical equation for the index of refraction of seawater." Applied optics **34**, 3477–80 (1995).

[138] M. N. Berberan-Santos, E. N. Bodunov, and B. Valeur, "Mathematical functions for the analysis of luminescence decays with underlying distributions 1. Kohlrausch decay function (stretched exponential)," Chemical Physics **315**, 171–182 (2005).

[139] D. C. Johnston, "Stretched exponential relaxation arising from a continuous sum of exponential decays," Physical Review B - Condensed Matter and Materials Physics **74** (2006).

[140] M. Cardona, R. V. Chamberlin, and W. Marx, "The history of the stretched exponential function," (2007).

[141] A. F. van Driel, I. S. Nikolaev, P. Vergeer, P. Lodahl, D. Vanmaekelbergh, and W. L. Vos, "Statistical analysis of time-resolved emission from ensembles of semiconductor quantum dots: Interpretation of exponential decay models," Physical Review B **75**, 035329 (2007).

[142] J. Wuttke, "Laplace-fourier transform of the stretched exponential function: Analytic error bounds, double exponential transform, and open-source implementation "libkww"," Algorithms **5**, 604–628 (2012).

[143] R. Kohlrausch, "Theorie des elektrischen Rückstandes in der Leidener Flasche," Annalen der Physik und Chemie **167**, 179–214 (1854).

[144] J. Davies, "The individual success of musicians, like that of physicists, follows a stretched exponential distribution," The European Physical Journal B - Condensed Matter **27**, 445–447 (2002).

[145] K. C. Lee, J. Siegel, S. E. Webb, S. Lévêque-Fort, M. J. Cole, R. Jones, K. Dowling, M. J. Lever, and P. M. French, "Application of the stretched exponential function to fluorescence lifetime imaging." Biophysical journal **81**, 1265–1274 (2001).

[146] F. Sangghaleh, B. Bruhn, T. Schmidt, and J. Linnros, "Exciton lifetime measurements on single silicon quantum dots." Nanotechnology **24**, 225204 (2013).

[147] G. Zatryb, a. Podhorodecki, J. Misiewicz, J. Cardin, and F. Gourbilleau, "On the nature of the stretched exponential photoluminescence decay for silicon nanocrystals." Nanoscale research letters **6**, 106 (2011).

[148] A. Irrera, F. Iacona, I. Crupi, C. D. Presti, G. Franzò, C. Bongiorno, D. Sanfilippo, G. D. Stefano, A. Piana, P. G. Fallica, A. Canino, and F. Priolo, "Electroluminescence and transport properties in amorphous silicon nanostructures," Nanotechnology **17**, 1428–1436 (2006).

[149] M. Berberan-Santos, E. N. Bodunov, and B. Valeur, "History of the Kohlrausch (stretched exponential) function: Pioneering work in luminescence," (2008).

[150] W. Liu, M. Howarth, A. B. Greytak, Y. Zheng, D. G. Nocera, A. Y. Ting, and M. G. Bawendi, "Compact Biocompatible Quantum Dots Functionalized for Cellular Imaging," (2008).

[151] K. A. Littau, P. J. Szajowski, A. J. Muller, A. R. Kortan, and L. E. Brus, "A luminescent silicon nanocrystal colloid via a high-temperature aerosol reaction," The Journal of Physical Chemistry **97**, 1224–1230 (1993).

[152] J. P. Wilcoxon, G. A. Samara, and P. N. Provencio, "Optical and electronic properties of Si nanoclusters synthesized in inverse micelles," Physical Review B **60**, 2704–2714 (1999).

[153] H.-J. Moon, G.-W. Park, S.-B. Lee, K. An, and J.-H. Lee, "Waveguide mode lasing via evanescent-wave-coupled gain from a thin cylindrical shell resonator," Applied Physics Letters **84**, 4547 (2004).

[154] P. Zijlstra, K. L. van der Molen, and A. P. Mosk, "Spatial refractive index sensor using whispering gallery modes in an optically trapped microsphere," Applied Physics Letters **90**, 161101 (2007).

[155] S. Pang, R. E. Beckham, and K. E. Meissner, "Quantum dot-embedded microspheres for remote refractive index sensing." Applied physics letters **92**, 221108–2211083 (2008).

[156] H. T. Beier, G. L. Coté, and K. E. Meissner, "Whispering gallery mode biosensors consisting of quantum dot-embedded microspheres." Annals of biomedical engineering **37**, 1974–83 (2009).

[157] M. Charlebois, a. Paquet, L. S. Verret, K. Boissinot, M. Boissinot, M. G. Bergeron, and C. N. Allen, "Toward automatic label-free whispering gallery modes biodetection with a quantum dot-coated microsphere population," Nanoscale Research Letters **5**, 524–532 (2010).

[158] A. François, K. J. Rowland, S. A. V, M. R. Henderson, and T. M. Monro, "Enhancing the radiation efficiency of dye doped whispering gallery mode microresonators," Optics Express **21**, 536–543 (2013).

[159] S. Lane, F. Marsiglio, Y. Zhi, and A. Meldrum, "Refractometric sensitivity and thermal stabilization of fluorescent core microcapillary sensors: theory and experiment." Applied optics **54**, 1331–40 (2015).

[160] S. McFarlane, "Fluorescent-core microcapillaries: Detection limits for biosensing applications," Master's thesis, University of Alberta, Edmonton, Alberta, Canada (2012).

[161] A. Meldrum and F. Marsiglio, "Capillary-Type Microfluidic Sensors Based on Optical Whispering Gallery Mode Resonances," Reviews in Nanoscience and Nanotechnology **3**, 193–209 (2014).

[162] J. Cras, C. Rowe-Taitt, D. Nivens, and F. Ligler, "Comparison of chemical cleaning methods of glass in preparation for silanization," Biosensors and Bioelectronics **14**, 683–688 (1999).

[163] V. Zamora, A. Díez, M. V. Andrés, and B. Gimeno, "Refractometric sensor based on whispering-gallery modes of thin capillaries," Optics express **15**, 12011–12016 (2007).

[164] M. Piliarik, P. Kvasnička, N. Galler, J. R. Krenn, and J. Homola, "Local refractive index sensitivity of plasmonic nanoparticles." Optics express **19**, 9213–9220 (2011).

[165] H. S. Dutta, A. K. Goyal, and P. Suchandan, "Sensitivity enhancement in photonic crystal waveguide platform for refractive index sensing applications," Journal of Nanophotonics **8** (2014).

[166] F. Sangghaleh, I. Sychugov, Z. Yang, J. G. C. Veinot, and J. Linnros, "Near-Unity Internal Quantum Efficiency of Luminescent Silicon Nanocrystals with Ligand Passivation." ACS nano **9**, 7097–104 (2015).